Cell Reports

Multiplatform Molecular Profiling Reveals Epigenomic Intratumor Heterogeneity in Ependymoma

Graphical Abstract

Stereotactic sampling of an anaplastic ependymoma
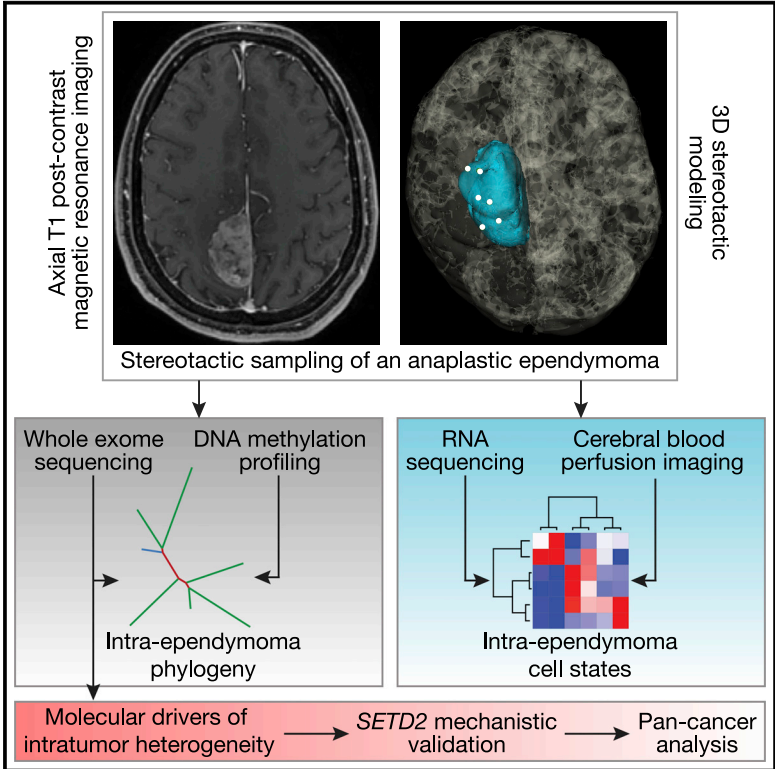
Authors

S. John Liu, Stephen T. Magill,
Harish N. Vasudevan, ...,
Michael W. McDermott,
Joseph F. Costello, David R. Raleigh

Correspondence

david.raleigh@ucsf.edu

In Brief

Tumor heterogeneity poses a barrier to cancer treatment. Liu et al. investigate radiographically distinct regions of an ependymoma tumor using transcriptomic, genetic, and epigenomic profiling and discover axes of gene expression programs that recapitulate normal brain development in addition to phylogenies that shed light on the tumorigenesis of ependymoma.

Highlights

- Epigenomic, transcriptomic, and exome profiles and phylogenies within an ependymoma

- Spatially distinct clusters reflect neuronal development gene expression programs

- Quantitative magnetic resonance imaging characteristics identify stem-like regions

- Mutant histone methyltransferase *SETD2* enhances proliferation in ependymoma cells

CellPress

# Multiplatform Molecular Profiling Reveals Epigenomic Intratumor Heterogeneity in Ependymoma

S. John Liu,[1,2,7] Stephen T. Magill,[1,2,7] Harish N. Vasudevan,[1,2,7] Stephanie Hilz,[2] Javier E. Villanueva-Meyer,[3] Sydney Lastella,[1,2] Vikas Daggubati,[1,2] Jordan Spatz,[2] Abrar Choudhury,[1,2] Brent A. Orr,[5] Benjamin Demaree,[6] Kyounghee Seo,[1,2] Sean P. Ferris,[4] Adam R. Abate,[6] Nancy Ann Oberheim Bush,[2] Andrew W. Bollen,[4] Michael W. McDermott,[2] Joseph F. Costello,[2] and David R. Raleigh[1,2,8,*]

[1]Department of Radiation Oncology, University of California, San Francisco, San Francisco, CA 94143, USA
[2]Department of Neurological Surgery, University of California, San Francisco, San Francisco, CA 94143, USA
[3]Department of Radiology and Biomedical Imaging, University of California, San Francisco, San Francisco, CA 94143, USA
[4]Department of Pathology, University of California, San Francisco, San Francisco, CA 94143, USA
[5]Department of Pathology, St. Jude Children's Research Hospital, Memphis, TN 38105, USA
[6]Department of Bioengineering and Therapeutic Sciences, California Institute for Quantitative Biosciences, University of California, San Francisco, San Francisco, CA 94158, USA
[7]These authors contributed equally
[8]Lead Contact
*Correspondence: david.raleigh@ucsf.edu
https://doi.org/10.1016/j.celrep.2020.01.018

SUMMARY

Ependymomas exist within distinct genetic subgroups, but the molecular diversity within individual ependymomas is unknown. We perform multiplatform molecular profiling of 6 spatially distinct samples from an ependymoma with *C11orf95-RELA* fusion. DNA methylation and RNA sequencing distinguish clusters of samples according to neuronal development gene expression programs that could also be delineated by differences in magnetic resonance blood perfusion. Exome sequencing and phylogenetic analysis reveal epigenomic intratumor heterogeneity and suggest that chromosomal structural alterations may precede accumulation of single-nucleotide variants during ependymoma tumorigenesis. In sum, these findings shed light on the oncogenesis and intratumor heterogeneity of ependymoma.

INTRODUCTION

Ependymal tumors of the central nervous system have diverse demographic, anatomic, radiologic, clinical, and molecular characteristics (Pajtler et al., 2015). There are 9 molecular subgroups of ependymomas (Pajtler et al., 2015), and the majority of supratentorial ependymomas harbor a genetic fusion between the uncharacterized gene *C11orf95* and the nuclear factor κB (NF-κB) transcriptional activator *RELA* (Pajtler et al., 2015; Parker et al., 2014). When expressed in neural stem cells, *C11orf95-RELA* is sufficient to induce ependymoma formation *in vivo*, suggesting that neural stem cells are a putative cell of origin for ependymal tumors (Ozawa et al., 2018; Taylor et al., 2005).

Molecular heterogeneity among ependymomas is well established (Capper et al., 2018; Johnson et al., 2010; Khatua et al.,

2017; Modena et al., 2006; Pajtler et al., 2015; Parker et al., 2014; Witt et al., 2011). In contrast, intratumor molecular heterogeneity within individual ependymal tumors is incompletely understood. In other central nervous system malignancies, intratumor heterogeneity encompassing cell composition, immune infiltration, and somatic mutations contributes to tumor growth and resistance to therapy (Müller et al., 2017; Parker et al., 2016; Patel et al., 2014; Szerlip et al., 2012; Yung et al., 1982). Thus, we hypothesized that molecular heterogeneity may exist within ependymoma and that understanding ependymoma heterogeneity may shed light on tumor development, patterns of recurrence, or potential therapeutic targets. To test these hypotheses, we performed multiplatform molecular profiling of 6 spatially distinct samples from a supratentorial anaplastic ependymoma with *C11orf95-RELA* fusion. Our findings reveal significant intratumor heterogeneity and a molecular phylogeny containing regionally distinct stem-like, neuronal differentiation, and immune-enriched regions within a single tumor. We discover that stem-like regions of ependymal tumors can be delineated on preoperative magnetic resonance perfusion and find that chromosomal copy number changes are an early molecular event in ependymoma tumorigenesis. Finally, we identify a previously uncharacterized missense mutation in the histone methyltransferase *SETD2* as an example of a potentially broader class of epigenomic modifiers of molecular heterogeneity within ependymoma.

RESULTS

Radiologic and Molecular Classification of Supratentorial Anaplastic Ependymoma with *C11orf95-RELA* Fusion

We collected 6 spatially distinct intraoperative samples from a 29-year-old male who initially presented to medical attention after experiencing a generalized seizure and was found to have a parasagittal mass on brain imaging (Figures 1A and 1B). Stereotactic analysis at the time of resection showed that samples were
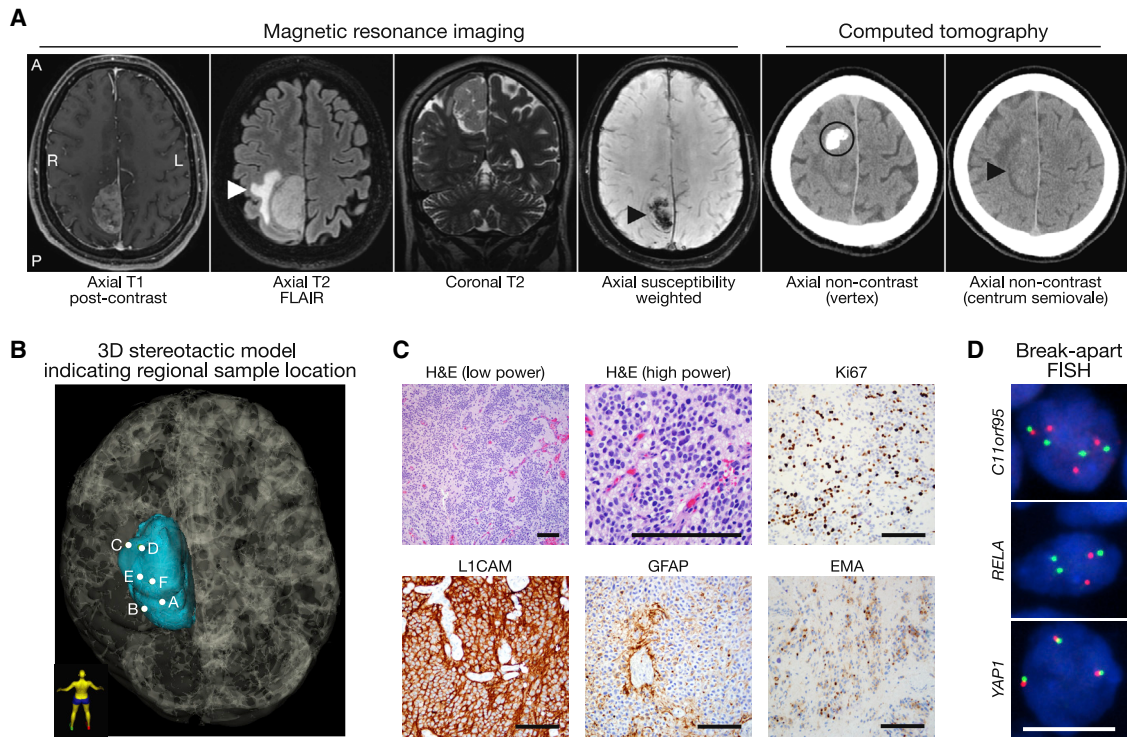
Figure 1. Radiologic and Molecular Classification of a Supratentorial Anaplastic Ependymoma with *C11orf95-RELA* Fusion

(A) Preoperative magnetic resonance imaging and computed tomography shows a right parasagittal heterogeneously enhancing mass with peritumoral edema (white arrowhead) and internal susceptibility (black arrowhead) that is distinct from a site of eccentric peripheral nodular calcification (black circle) and therefore suggestive of internal hemorrhage. Of note, a significant difference in head tilt and imaging gantry influences the appearance of tumor location as denoted by black arrowheads in images 4 and 6. A, anterior; FLAIR, fluid-attenuated inversion recovery; L, left; P, posterior; R, right.

(B) 3D stereotactic mapping of 6 samples (A–F) obtained for this study. Patient orientation is represented by the model in bottom left.

(C) Low- and high-power hematoxylin and eosin (H&E) images and immunohistochemical stains demonstrating strong L1CAM positivity, GFAP positivity in cytoplasmic processes of perivascular pseudorosettes, paranuclear dot-like and ring-like EMA positivity, and a Ki-67 labeling index of 20%, all features that support the diagnosis of anaplastic ependymoma, WHO grade III. Black scale bars, 100 μm.

(D) Break-apart fluorescence *in situ* hybridization (FISH) (red and green probes) shows rearrangement of *C11orf95* and *RELA*, but not *YAP1*. Nuclei are shown in blue. White scale bar, 10 μm.

separated by a median of 1.7 cm (range 0.6–3.4 cm) and were closer to the periphery of the tumor than to the centroid (Figure S1). A separate sample that was designated for clinical pathology was diagnosed as anaplastic ependymoma, World Health Organization (WHO) grade III, with a mitotic count of 15 mitoses per 10 high-power fields, a Ki-67 labeling index of 20%, and strong L1CAM cytoplasmic and membrane staining, consistent with *C11orf95-RELA* fusion (Figure 1C). Targeted DNA sequencing using a Clinical-Laboratory-Improvement-Amendment-certified panel of 510 cancer-associated genes (Kline et al., 2017) showed multiple segmental copy number variations along chromosome 11q consistent with chromothripsis (Figure S2A). Break-apart DNA fluorescence *in situ* hybridization demonstrated rearrangement of *RELA* and *C11orf95*, but not *YAP1* (Figure 1D), a gene fused to *C11orf95* in a minority of supratentorial ependymomas (Parker et al., 2014).

Cortical Development and Differentiation Gene Expression Programs Define Intratumor Heterogeneity in Ependymoma

We performed RNA sequencing (RNA-seq) of the 6 samples to delineate gene expression heterogeneity. Pooled analysis of all samples using two independent fusion gene detectors identified an in-frame fusion between exon 2 of *C11orf95* and exon 2 of *RELA* (Figure S2B), corresponding to the pathogenic *RELA*[FUS1] fusion found in the majority of supratentorial ependymomas (Parker et al., 2014). No other fusion genes were concordantly detected by both methods, and the 6 samples expressed similar levels of *L1CAM*, *CCND1*, *C11orf95*, and *RELA* (Figure S2C), each of which are specific markers of *C11orf95-RELA* ependymoma (Parker et al., 2014).

Principal-component analysis (PCA) was performed to separate the 6 samples based on gene expression variability (Figure 2A). The most variable genes in PCA space were used for hierarchical clustering, revealing 3 clusters of samples (Figure 2B). To identify drivers of intratumor heterogeneity, we ranked genes based on their loading scores for the first three principal components (Figure 2C). Gene Ontology analysis (Figure S2D) showed that genes in axis 1 (samples C and D) were enriched for the *OLIG1* and *OLIG2* co-expression networks (p = 0.01 and 0.04, respectively), which are implicated in stem-like identity in glioma (Aguirre-Cruz et al., 2004; Ligon et al., 2004, 2007) and early phases of glial cell development (Novitch et al., 2001; Zhou
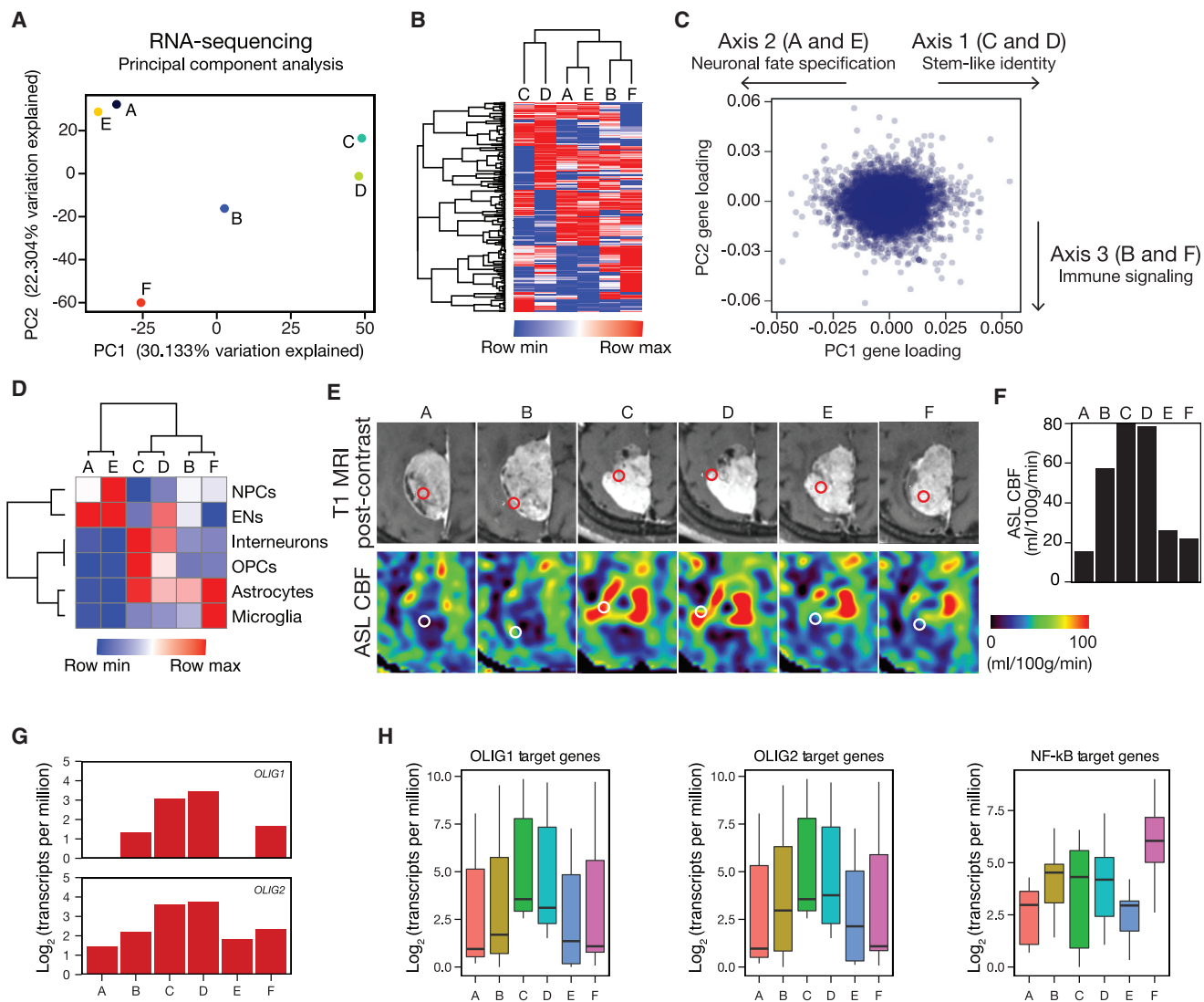
Figure 2. Cortical Development and Differentiation Gene Expression Programs Define Intratumor Heterogeneity in an Ependymoma

(A) Principal-component analysis (PCA) of RNA-seq data reveal that 52% percent of variation among regional samples is explained by the first two principal components. PC, principal component.

(B) Hierarchical clustering of samples using the top 250 most variable genes in RNA-seq identifies 3 subgroups.

(C) Scatterplot of gene loading scores in PCA with arrows indicating axes used for gene ranking.

(D) Gene expression heatmap of cell-type-specific genes in the developing human cerebral cortex (Zhong et al., 2018) recapitulates the same clusters as unbiased transcriptome-wide analysis. EN, excitatory neurons; NPCs, neural progenitor cells; OPCs, oligodendrocyte progenitor cells.

(E and F) Preoperative T1 post-contrast and arterial spin labeling perfusion (E) and quantitative arterial spin labeling perfusion (F) of stereotactically defined regions demonstrate enhanced cerebral blood flow in regions with stem-like identity (C and D). Red and white circles indicate sample locations. ASL, arterial spin labeling; CBF, cerebral blood flow; MRI, magnetic resonance imaging.

(G) *OLIG1* and *OLIG2*, which are implicated in stem-like identity in glioma and early phases of glial cell development, are enriched in samples C and D (*OLIG1* p = 0.007; *OLIG2* p = 0.002; Student's t test).

(H) Analysis of published OLIG1, OLIG2, and NF-κB target genes reveals enrichment of OLIG1 (p = 9.5×10^{-6}) and OLIG2 (p = 0.00045) targets in stem-like samples C and D and enrichment of NF-κB targets in samples B and F (p = 0.00093), consistent with underlying activity of the *C11orf95-RELA* pathogenic fusion gene (Kolmogorov-Smirnov test).

and Anderson, 2002). In contrast, genes in axis 2 (samples A and E) were enriched for the *TSHZ3* and *LHX9* co-expression networks (p = 0.04 for each), which are involved in neuronal fate specification in normal development (Bertuzzi et al., 1999; Caubit et al., 2016; 2010; Liu et al., 2015; Peukert et al., 2011; Rétaux et al., 1999). Genes in axis 3 (samples B and F) were enriched for *RELA* target genes, including *CXCL2* and *HSPA1A* (p < 0.0001 for each), which are suggestive of immune signaling (Hayden and Ghosh, 2008; Karin et al., 2002) and underlying activity of the *C11orf95-RELA* pathogenic fusion gene.
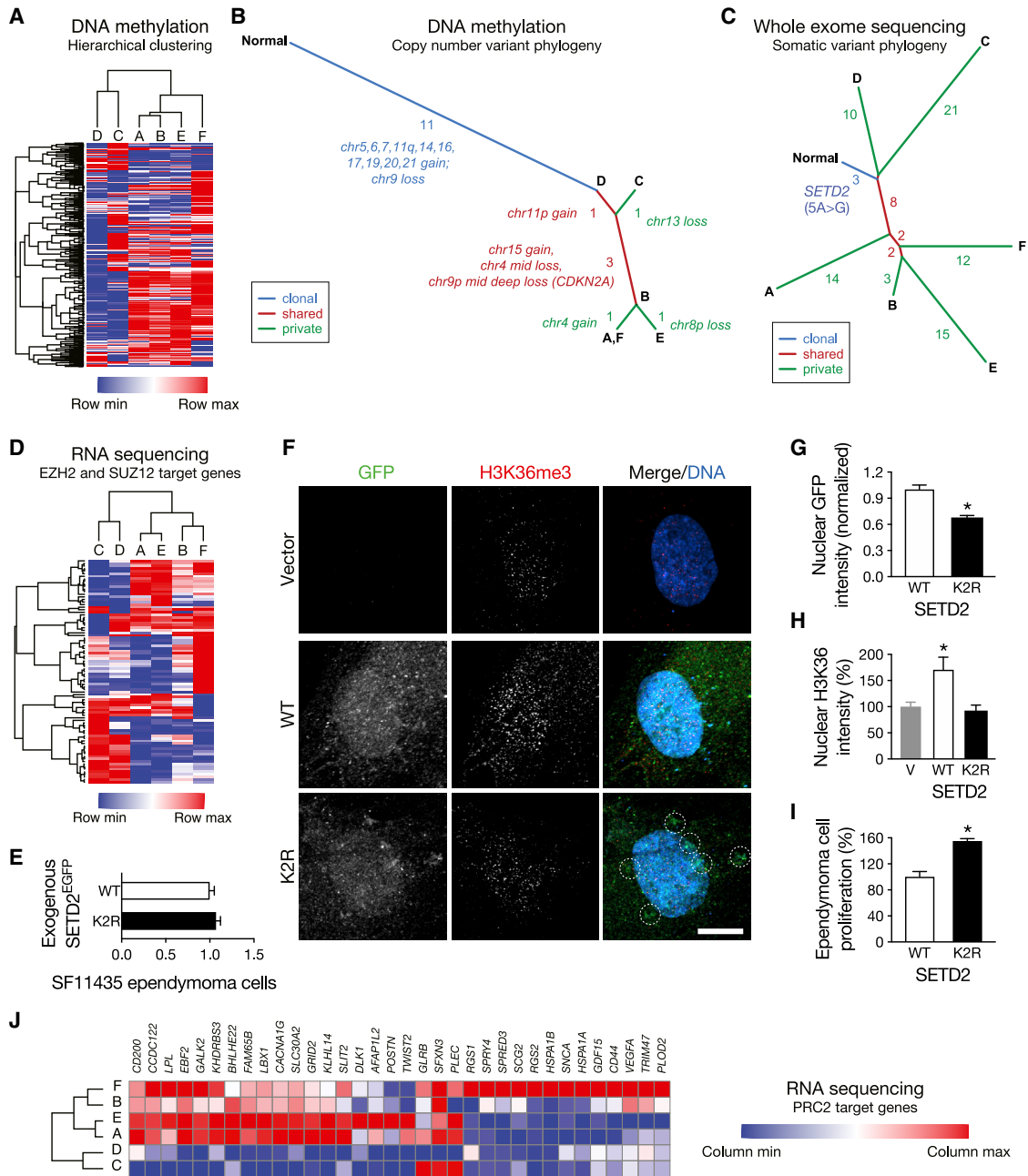
Figure 3. Phylogenetic Analysis Identifies Early Chromosome Structural Alterations and Epigenomic Intratumor Heterogeneity in Ependymoma

(A) Hierarchical clustering of regional samples using the top 2,000 most variable methylation probes closely recapitulates gene-expression-based clustering.

(B) Intratumor phylogeny based on clonal ordering of copy number variants derived from methylation analysis suggests that chromosomal structural alterations are an early event during ependymoma tumorigenesis. The number and identity of copy number variants defining each axis are indicated.

(C) Intratumor phylogeny based on clonal ordering of somatic variants suggests an epigenomic contribution to molecular heterogeneity. The number of somatic variants defining each axis is indicated.

(D) Hierarchical clustering restricted to highly variable *EZH2* and *SUZ12* target gene expression recapitulates the same clusters of samples as unbiased transcriptome-wide analysis.

(E) Confocal microscopy of total cellular fluorescence demonstrated equivalent expression of fluorescent fusions of SETD2^{K2R} (K2R) and wild-type SETD2 (WT).

(F–H) K2R fused to EGFP demonstrates diminished nuclear qualitative (F) and quantitative (G) localization and increased perinuclear aggregation (dotted circles) relative to WT fused to EGFP in SF11435 anaplastic ependymoma cells. Consistently, WT overexpression increases qualitative (F) and quantitative (H) nuclear H3K36me3 intensity relative to vector (V) and K2R overexpression. SETD2 constructs are shown in green, H3K36me3 chromatin marks are shown in red, and nuclei are marked with Hoechst 3342 in blue. Quantitative data are normalized to control. Scale bar, 10 μm. *p < 0.0001; Student's t test.

(legend continued on next page)

Supratentorial ependymomas have been proposed to arise from radial glia neural stem cells (Taylor et al., 2005), and we discovered that developmental gene expression programs defined intratumor heterogeneity in ependymoma (Figures 2C and 2D). Thus, we hypothesized that clusters of samples would show molecular similarity to cell types in the developing brain (Nowakowski et al., 2017). To test that hypothesis, we quantified the mean expression signatures of marker genes for the major cell types in the developing cerebral cortex in each sample (Zhong et al., 2018). Consistent with PCA gene enrichment analysis, samples C and D were enriched for oligodendrocyte progenitor cell, astrocyte, and interneuron markers; samples A and E were enriched for neural progenitor cell and excitatory neuron markers; samples B and F were enriched for astrocyte markers; and sample F was further enriched for microglia markers (Figure 2D).

To determine whether preoperative imaging could distinguish between regions of molecular heterogeneity in ependymoma, we performed quantitative magnetic resonance imaging and compared differences between sample locations. Arterial spin labeling measurement of perfusion revealed that stem-like regions C and D exhibited elevated cerebral blood flow compared to other regions (Figures 2E and 2F). On diffusion tensor imaging, regions C and D had elevated fractional anisotropy, likely relating to differences in cellular architecture given the similar cellularity across the samples (Figures S2E, S2F, and S4D). Further, we found that sample F, which was closest to the tumor centroid (Figure S1A), had low cerebral blood flow (Figure 2E) and was enriched in *HSPA1A* by RNA-seq (Figure S2G), a transcriptional target of *RELA* that is implicated in prolonged hypoxia (Lewis et al., 1999; Rahat et al., 2011). Consistently, sample F was enriched in an immune gene expression program (Figures 2C and S2D) characteristic of microglia (Figure 2D), and hypoxia is an important regulator of immune activation (Lewis et al., 1999; Rahat et al., 2011). Cellular metabolism is also known to impact chromatin modification, and differential expression analysis revealed that the histone deacetylase gene *HDAC9* was suppressed in samples C and D (Figure S3), the regions with the highest cerebral blood flow (Figures 2E and 2F).

To further investigate the putative stem-like markers identified in samples C and D, we investigated the expression of *OLIG1* and *OLIG2* and found that both were enriched in stem-like regions relative to other samples (Figure 2G). We also analyzed the expression levels of *OLIG1* and *OLIG2* target genes from the ARCHS4 database (Lachmann et al., 2018) that were highly variable in our RNA-seq data and found that these targets were also increased in samples C and D (Figure 2H). Conversely, we found elevated expression of highly variable *RELA* targets in samples B and F (Figure 2H), which is likely reflective of the underlying activity of the *C11orf95-RELA* pathogenic fusion gene (Kuleshov et al., 2016). These data are consistent with the hypothesis that regional variation in *OLIG1* and *OLIG2* expression and NF-kB pathway activation underlie intratumor heterogeneity in ependymoma. Moreover, our findings suggest that, in this

ependymoma, intratumor heterogeneity is defined by neuronal development and immunologic gene expression programs that can be delineated by quantitative preoperative imaging characteristics.

Epigenomic Profiling of Intratumor Heterogeneity in Ependymoma Corroborates Neuronal Development Signatures

To validate our gene-expression-based clustering results, we applied PCA toward 850K DNA methylation profiles of the 6 samples. DNA-methylation-based clustering paralleled RNA-seq results and delineated regions C and D from the remaining regions in the first principal component (Figure S4A). Hierarchical clustering of the most variable methylation probes further revealed 3 clusters that were concordant to those obtained using RNA-seq (Figures 2B and 3A). Analysis of signature probes showed that sites of hypomethylation in samples C and D were associated with stem cell genes (false discovery rate [FDR] = 0.016; Figure S4B). Finally, we applied DNA methylation profiles to a methylation-based random forest classifier (Capper et al., 2018) to confirm that each sample unambiguously classified as *RELA* fusion ependymoma (Figure S4C).

Phylogenetic Analysis Identifies Early Chromosome Structural Alterations and Epigenomic Intratumor Heterogeneity in Ependymoma

To assess clonal relationships between the 6 samples, we performed phylogenetic ordering of copy number variation (CNV) profiles derived from methylation arrays. Eleven of 18 CNVs detected were common to all regions, although samples enriched in differentiation gene expression programs (A, B, E, and F) exhibited more CNVs than stem-like samples (C and D; Figure 3B; Table S1).

To determine whether differences in somatic variants may underlie intratumor heterogeneity in ependymoma, we performed exome sequencing of the 6 samples and matched normal DNA from peripheral blood. Consistent with diffusion tensor imaging (Figures S2E and S2F), cellularity and ploidy analyses from exome sequencing revealed little variability across ependymoma samples (cellularity range: 0.75–0.9; ploidy range: 3.4–3.5), suggesting equivalent proportions of tumor cells in each region (Figure S4D). Importantly, phylogenetic ordering of CNVs derived from exome sequencing was concordant with methylation-derived CNVs (Figure S4E; Table S1).

We identified 102 somatic variants (single-nucleotide variants and indels) from exome sequencing across all 6 samples, among which 3 were common to all samples and 75 were private to individual samples (Table S1). Forty-one variants were described in the COSMIC database (Forbes et al., 2017), and 15 were predicted to be pathogenic (Shihab et al., 2013). In contrast to CNVs, phylogenetic ordering of somatic variants revealed early divergence of the 6 samples (Figure 3C; Johnson et al., 2014). One of the earliest somatic variants that was detected in all

---

(I) K2R overexpression in SF11435 cells increases cell proliferation relative to WT overexpression. Data are representative of 3 biologic replicates and are normalized to cell proliferation with WT overexpression. *p < 0.0001; Student's t test.

(J) PRC2 target genes are depleted in regions with higher allelic frequency of *SETD2*^{K2R} (C and D), consistent with antagonism between H3K36me3 and PRC2 gene silencing.
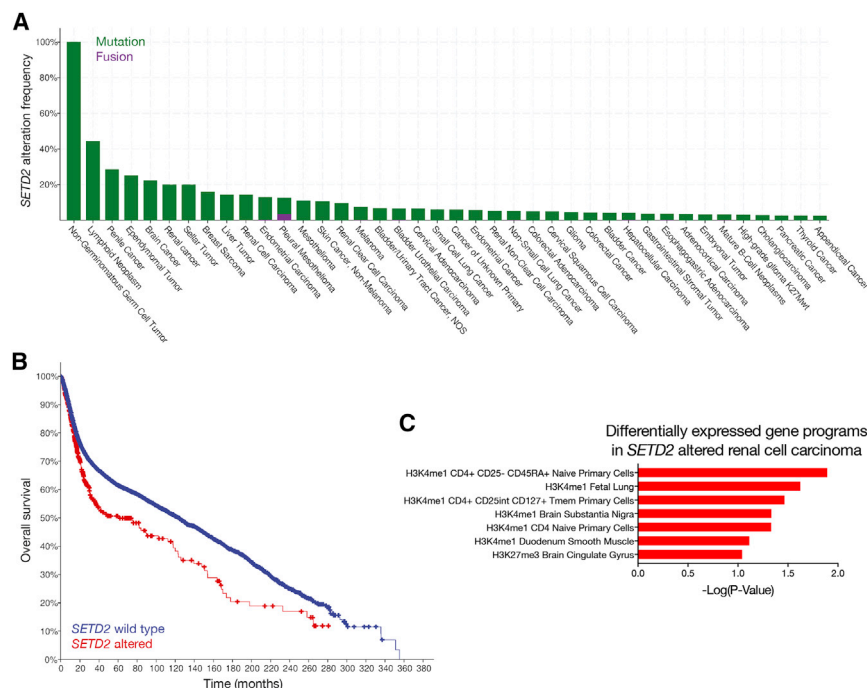
Figure 4. Mutation of the Epigenomic Regulator *SETD2* Is Associated with Adverse Outcomes across All Cancers

(A) Analysis of 42,199 samples from cBioPortal reveals 1,548 cancers with *SETD2* alteration, representing 3.7% of all cases. The 40 most common cancers with *SETD2* alterations are shown, with omission of 93 additional cancer types with known *SETD2* alterations at lower frequencies.

(B) Patients from cBioPortal with *SETD2* mutant cancers have lower overall survival compared to patients with *SETD2* wild-type cancers (p = 0.000017; log rank test).

(C) Ontology analysis of differentially expressed genes in 276 renal cell carcinomas from cBioPortal with genetic or transcriptional alterations *SETD2*, compared to 258 renal cell carcinomas with wild-type *SETD2*, reveals heterogeneous gene expression programs that are normally reserved for CD4 T cells, fetal lung, brain cingulate gyrus, brain substantia nigra, and smooth muscle. In contrast, renal cell carcinomas with wild-type *SETD2* are enriched in gene expression programs associated with penis foreskin primary cells and regulatory T (T reg) primary cells.

samples was a 5A > G (p.K2R) missense substitution in the histone methyltransferase *SETD2*. Inactivating mutations in *SETD2* are implicated in diverse pediatric brain tumors (Fontebasso et al., 2013), and we confirmed the *SETD2^{K2R}* mutation in all tumor samples, but not in peripheral blood, by targeted DNA sequencing (Figure S4F). Remarkably, the highest mutant allele frequencies of *SETD2^{K2R}* were detected in regions C (0.282) and D (0.352), the samples defined by stem cell transcriptional networks (Figure S2D).

To elucidate the molecular impact of *SETD2^{K2R}*, we asked whether gene expression programs distinguishing clusters of samples were enriched for targets of epigenomic regulators. Genes in axis 2 (samples A and E) were enriched for targets of *SUZ12* (p = 0.00001) and *EZH2* (p = 0.001), both of which are critical components of the polycomb repressive complex 2 (PRC2) (Figure S4G). PRC2 is an epigenomic regulator that is antagonistic to SETD2 (Lachmann et al., 2010), and the allelic frequency of *SETD2^{K2R}* was lower in samples defined by neuronal differentiation gene expression programs (A, B, E, and F; mean 0.244). Consistently, hierarchical clustering using only expression of highly variable PRC2 target genes recapitulated the same clusters as unbiased transcriptome-wide analysis (Figure 3D), suggesting an epigenomic contribution to intratumor molecular heterogeneity in ependymoma.

To investigate the functional impact of the K2R substitution, we overexpressed fluorescent fusions of wild-type *SETD2* and *SETD2* with the 5A > G substitution (*SETD2^{K2R}*) in supratentorial anaplastic ependymoma cells with *RELA* fusion (Figure 3E). The K2R substitution is within the nuclear localization sequence of SET2, and consistently, SETD2^{K2R} displayed diminished nuclear intensity and increased perinuclear aggregation compared to wild-type SETD2 (Figures 3F and 3G). Consistent with the chromatin-modifying function of SETD2, overexpression of wild-type

SETD2 increased nuclear H3K36me3 intensity, but *SETD2^{K2R}* did not (Figure 3H). Moreover, *SETD2^{K2R}* overexpression increased cell proliferation and viability relative to wild-type *SETD2* overexpression (Figure 3I).

SETD2 is the primary methyltransferase for histone H3 lysine 36 (H3K36), a chromatin mark associated with active transcriptional elongation (Kolasinska-Zwierz et al., 2009; Kouzarides, 2007). H3K36 methylation antagonizes histone H3 lysine (H3K27) methylation (Yuan et al., 2011), a chromatin mark that is induced by PRC2 and is associated with gene repression (Kouzarides, 2007). As nuclear localization of *SETD2^{K2R}* is impaired (Figures 3F and 3G), we hypothesized that regions with higher allelic frequency of *SETD2^{K2R}* would show greater gene silencing by PRC2. To test that hypothesis, we analyzed the expression of PRC2 target genes and found that many candidates were suppressed in regions with higher allelic frequency of *SETD2^{K2R}* (C and D), consistent with antagonism between SETD2 transcriptional elongation and PRC2 gene silencing (Figure 3J). In sum, these data support epigenomic misregulation as a contributing factor to ependymoma cell proliferation and suggest that this paradigm may be particularly important in regions defined by stem cell transcriptional networks.

Mutation of the Epigenomic Regulator *SETD2* Is Associated with Adverse Outcomes across All Cancers

Although *SETD2* is not recurrently mutated in ependymoma (Mack et al., 2018), we hypothesized that mutation of epigenomic regulators may be a common feature of molecularly heterogeneous tumors and could therefore represent a biomarker of adverse outcomes in cancer. To test that hypothesis, we queried 42,199 samples across all human cancers and identified 1,548 tumors with *SET2D2* mutations, representing a surprising 3.7% of all cases (Figure 4A; Gao et al., 2013). Consistent with the

prognostic significance of *SETD2* mutation in pediatric high-grade glioma (Fontebasso et al., 2013; Mackay et al., 2017), patients with *SETD2* mutant cancers exhibited significantly lower overall survival compared to patients with *SETD2* wild-type cancers (Figure 4B). In contrast to ependymoma, genetic or transcriptomic alterations in *SETD2* are identified in a remarkable 52% of renal cell carcinomas (Ricketts et al., 2018). Thus, we compared differentially expressed genes in 534 renal cell carcinomas with and without alterations in *SETD2* and found that tumors with *SETD2* alterations were enriched in heterogeneous gene expression programs that are normally reserved for CD4 T cells, fetal lung, brain cingulate gyrus, brain substantia nigra, and smooth muscle (Figure 4C). In sum, these data support a greater paradigm of epigenomic dysregulation as a regulator of intratumor heterogeneity and, in conjunction with our findings in ependymoma, suggest that regional differences in chromatin architecture may promote tumor growth and resistance to therapy.

DISCUSSION

We find that transcriptional signatures of molecular compartments in this ependymoma recapitulate critical aspects of human cerebral cortex development. Remarkably, gene expression programs associated with oligodendrocyte progenitor cells, neural progenitor cells, and mature microglia are spatially distinct within this tumor. These data are consistent with the observation that supratentorial ependymomas are associated with gene expression profiles of the embryonic brain (Johnson et al., 2010) and are also enriched in neural differentiation genes, such as *LHX2* and *FOXG1* (Andreiuolo et al., 2010). Moreover, our results in ependymoma are reminiscent of embryonal brain tumors and other pediatric cancers, which are also associated with misactivation of signaling pathways that are critical for central nervous system development.

The $SETD2^{K2R}$ point substitution we report has been described in acute lymphoblastic leukemia, where its functional consequences are unknown (Mar et al., 2014). We hypothesize that regional differences in gene dosage regulate nuclear localization of SETD2, resulting in heterogeneous chromatin states within ependymoma that promote distinct developmental or differentiation gene expression programs to maintain or suppress a stem-like state, respectively. Indeed, H3K27 methylation at CpG islands can lead to a hypermethylated state that is associated with malignant transformation (Ohm et al., 2007; Schlesinger et al., 2007; Widschwendter et al., 2007). Consistently, we find that PRC2 activity is increased in ependymoma regions with higher allelic frequency of $SETD2^{K2R}$. Notably, *SETD2* is not recurrently mutated in ependymoma, but in the context of lower overall survival for *SETD2* mutant cancers than *SETD2* wild-type malignancies, we speculate that our discovery of *SETD2* mutation as an epigenomic feature of molecular heterogeneity in an ependymoma may represent a foundational discovery supporting a greater paradigm in ependymoma and other tumors. Modeling these findings, however, is challenging. Reductionist cell culture systems are poorly suited to comprehensive investigations of intratumor heterogeneity, and primary tissues are not amenable to mechanistic studies that might identify molecular drivers of heterogeneity. Further, we cannot exclude the possi-

bility that intratumor heterogeneity in RNA transcription or DNA methylation were a consequence of driver events not captured by our current study, such as mutation of non-coding regions within the genome (Weinhold et al., 2014). We acknowledge that profiling multiple regions from a single tumor will not fully reflect tumor heterogeneity in all ependymomas. Future studies will be aimed at extending our findings across additional ependymomas and correlating them with clinical outcomes. Nonetheless, epigenomic variability resulting in intratumor heterogeneity has been postulated for other malignancies (Ohlsson et al., 2003) and represents a compelling process that may have important implications for targeted therapies for ependymoma patients. Indeed, epigenomic regulators are frequently mutated in ependymoma (Huether et al., 2014), and epigenomic alterations define lethal pediatric ependymomas without identifiable recurrent mutations (Mack et al., 2014). Further, intratumor heterogeneity is a significant source of resistance to cancer treatment (Levine et al., 2019; Watkins and Schwarz, 2018), and histone modifiers function as drivers of cellular heterogeneity and resistance to molecular therapy (Hinohara et al., 2018). Thus, our discovery of a heterogeneously expressed epigenomic regulator of ependymoma cell proliferation suggests that such genes could play a crucial role in modulating tumor sensitivity to both traditional ependymoma therapies and molecular agents.

STAR★METHODS

Detailed methods are provided in the online version of this paper and include the following:

- KEY RESOURCES TABLE
- LEAD CONTACT AND MATERIALS AVAILABILITY
- EXPERIMENTAL MODEL AND SUBJECT DETAILS
  - Cell Culture
  - Tumor sample acquisition
- METHOD DETAILS
  - Quantitative imaging analysis
  - Sample distance metric analysis
  - Tissue processing and immunohistochemistry
  - Fluorescence *In Situ* Hybridization (FISH)
  - RNA-seq
  - DNA Methylation Arrays
  - Whole exome sequencing
  - Sanger sequencing
  - Phylogenetic analysis
  - SETD2 cloning
  - Microscopy and proliferation assays
- QUANTIFICATION AND STATISTICAL ANALYSIS
- DATA AND CODE AVAILABILITY

SUPPLEMENTAL INFORMATION

Supplemental Information can be found online at https://doi.org/10.1016/j.celrep.2020.01.018.

AUTHOR CONTRIBUTIONS

S.J.L., S.T.M., H.N.V., S.H., J.E.V.-M., S.L., V.D., J.S., A.C., K.S., and D.R.R. designed research studies, conducted experiments, acquired data, analyzed data, and wrote the manuscript. S.P.F. and B.A.O. conducted experiments, acquired data, and analyzed data. N.A.O.B., A.W.B., M.W.D., B.D., A.R.A., and J.F.C. analyzed data, acquired data, and provided reagents. All authors critically revised the manuscript and approved final submission.

DECLARATION OF INTERESTS

The authors declare no competing interests.

REFERENCES

Aguirre-Cruz, L., Mokhtari, K., Hoang-Xuan, K., Marie, Y., Criniere, E., Taillibert, S., Lopes, M., Delattre, J.-Y., and Sanson, M. (2004). Analysis of the bHLH transcription factors Olig1 and Olig2 in brain tumors. J. Neurooncol. 67, 265–271.

Andreiuolo, F., Puget, S., Peyre, M., Dantas-Barbosa, C., Boddaert, N., Philippe, C., Mauguen, A., Grill, J., and Varlet, P. (2010). Neuronal differentiation distinguishes supratentorial and infratentorial childhood ependymomas. Neuro-oncol. 12, 1126–1134.

Aryee, M.J., Jaffe, A.E., Corrada-Bravo, H., Ladd-Acosta, C., Feinberg, A.P., Hansen, K.D., and Irizarry, R.A. (2014). Minfi: a flexible and comprehensive Bioconductor package for the analysis of Infinium DNA methylation microarrays. Bioinformatics 30, 1363–1369.

Bertuzzi, S., Porter, F.D., Pitts, A., Kumar, M., Agulnick, A., Wassif, C., and Westphal, H. (1999). Characterization of Lhx9, a novel LIM/homeobox gene expressed by the pioneer neurons in the mouse cerebral cortex. Mech. Dev. 81, 193–198.

Bray, N.L., Pimentel, H., Melsted, P., and Pachter, L. (2016). Near-optimal probabilistic RNA-seq quantification. Nat. Biotechnol. 34, 525–527.

Capper, D., Jones, D.T.W., Sill, M., Hovestadt, V., Schrimpf, D., Sturm, D., Koelsche, C., Sahm, F., Chavez, L., Reuss, D.E., et al. (2018). DNA methylation-based classification of central nervous system tumours. Nature 555, 469–474.

Caubit, X., Thoby-Brisson, M., Voituron, N., Filippi, P., Bévengut, M., Faralli, H., Zanella, S., Fortin, G., Hilaire, G., and Fasano, L. (2010). Teashirt 3 regulates development of neurons involved in both respiratory rhythm and airflow control. J. Neurosci. 30, 9465–9476.

Caubit, X., Gubellini, P., Andrieux, J., Roubertoux, P.L., Metwaly, M., Jacq, B., Fatmi, A., Had-Aissouni, L., Kwan, K.Y., Salin, P., et al. (2016). TSHZ3 deletion causes an autism syndrome and defects in cortical projection neurons. Nat. Genet. 48, 1359–1369.

Chen, E.Y., Tan, C.M., Kou, Y., Duan, Q., Wang, Z., Meirelles, G.V., Clark, N.R., and Ma'ayan, A. (2013). Enrichr: interactive and collaborative HTML5 gene list enrichment analysis tool. BMC Bioinformatics 14, 128.

Cingolani, P., Platts, A., Wang, L., Coon, M., Nguyen, T., Wang, L., Land, S.J., Lu, X., and Ruden, D.M. (2012). A program for annotating and predicting the effects of single nucleotide polymorphisms, SnpEff: SNPs in the genome of Drosophila melanogaster strain w1118; iso-2; iso-3. Fly (Austin) 6, 80–92.

Davidson, N.M., Majewski, I.J., and Oshlack, A. (2015). JAFFA: high sensitivity transcriptome-focused fusion gene detection. Genome Med. 7, 43.

Desper, R., and Gascuel, O. (2002). Fast and accurate phylogeny reconstruction algorithms based on the minimum-evolution principle. J. Comput. Biol. 9, 687–705.

Du, P., Zhang, X., Huang, C.-C., Jafari, N., Kibbe, W.A., Hou, L., and Lin, S.M. (2010). Comparison of Beta-value and M-value methods for quantifying methylation levels by microarray analysis. BMC Bioinformatics 11, 587.

Favero, F., Joshi, T., Marquard, A.M., Birkbak, N.J., Krzystanek, M., Li, Q., Szallasi, Z., and Eklund, A.C. (2015). Sequenza: allele-specific copy number and mutation profiles from tumor sequencing data. Ann. Oncol. 26, 64–70.

Fontebasso, A.M., Schwartzentruber, J., Khuong-Quang, D.-A., Liu, X.-Y., Sturm, D., Korshunov, A., Jones, D.T.W., Witt, H., Kool, M., Albrecht, S., et al. (2013). Mutations in SETD2 and genes affecting histone H3K36 methylation target hemispheric high-grade gliomas. Acta Neuropathol. 125, 659–669.

Forbes, S.A., Beare, D., Boutselakis, H., Bamford, S., Bindal, N., Tate, J., Cole, C.G., Ward, S., Dawson, E., Ponting, L., et al. (2017). COSMIC: somatic cancer genetics at high-resolution. Nucleic Acids Res. 45 (D1), D777–D783.

Fortin, J.-P., Labbe, A., Lemire, M., Zanke, B.W., Hudson, T.J., Fertig, E.J., Greenwood, C.M., and Hansen, K.D. (2014). Functional normalization of 450k methylation array data improves replication in large cancer studies. Genome Biol. 15, 503.

Fortin, J.-P., Triche, T.J., Jr., and Hansen, K.D. (2017). Preprocessing, normalization and integration of the Illumina HumanMethylationEPIC array with minfi. Bioinformatics 33, 558–560.

Gao, J., Aksoy, B.A., Dogrusoz, U., Dresdner, G., Gross, B., Sumer, S.O., Sun, Y., Jacobsen, A., Sinha, R., Larsson, E., et al. (2013). Integrative analysis of complex cancer genomics and clinical profiles using the cBioPortal. Sci. Signal. 6, pl1.

Garrison, E., and Marth, G. (2012). Haplotype-based variant detection from short-read sequencing. arXiv, arXiv:1207.3907v2. https://arxiv.org/abs/1207.3907.

Harrow, J., Frankish, A., Gonzalez, J.M., Tapanari, E., Diekhans, M., Kokocinski, F., Aken, B.L., Barrell, D., Zadissa, A., Searle, S., et al. (2012). GENCODE: the reference human genome annotation for The ENCODE Project. Genome Res 22, 1760–1774.

Hayden, M.S., and Ghosh, S. (2008). Shared principles in NF-kappaB signaling. Cell 132, 344–362.

Hinohara, K., Wu, H.-J., Vigneau, S., McDonald, T.O., Igarashi, K.J., Yamamoto, K.N., Madsen, T., Fassl, A., Egri, S.B., Papanastasiou, M., et al. (2018). KDM5 histone demethylase activity links cellular transcriptomic heterogeneity to therapeutic resistance. Cancer Cell 34, 939–953.e9.

Huether, R., Dong, L., Chen, X., Wu, G., Parker, M., Wei, L., Ma, J., Edmonson, M.N., Hedlund, E.K., Rusch, M.C., et al. (2014). The landscape of somatic mutations in epigenetic regulators across 1,000 paediatric cancer genomes. Nat. Commun. 5, 3630.

Johnson, R.A., Wright, K.D., Poppleton, H., Mohankumar, K.M., Finkelstein, D., Pounds, S.B., Rand, V., Leary, S.E.S., White, E., Eden, C., et al. (2010). Cross-species genomics matches driver mutations and cell compartments to model ependymoma. Nature 466, 632–636.

Johnson, B.E., Mazor, T., Hong, C., Barnes, M., Aihara, K., McLean, C.Y., Fouse, S.D., Yamamoto, S., Ueda, H., Tatsuno, K., et al. (2014). Mutational analysis reveals the origin and therapy-driven evolution of recurrent glioma. Science 343, 189–193.

Karin, M., Cao, Y., Greten, F.R., and Li, Z.-W. (2002). NF-kappaB in cancer: from innocent bystander to major culprit. Nat. Rev. Cancer 2, 301–310.

Khatua, S., Ramaswamy, V., and Bouffet, E. (2017). Current therapy and the evolving molecular landscape of paediatric ependymoma. Eur. J. Cancer 70, 34–41.

Kim, D., Pertea, G., Trapnell, C., Pimentel, H., Kelley, R., and Salzberg, S.L. (2013). TopHat2: accurate alignment of transcriptomes in the presence of insertions, deletions and gene fusions. Genome Biol. 14, R36.

Kline, C.N., Joseph, N.M., Grenert, J.P., van Ziffle, J., Talevich, E., Onodera, C., Aboian, M., Cha, S., Raleigh, D.R., Braunstein, S., et al. (2017). Targeted next-generation sequencing of pediatric neuro-oncology patients improves

diagnosis, identifies pathogenic germline mutations, and directs targeted therapy. Neuro-oncol. *19*, 699–709.

Koboldt, D.C., Zhang, Q., Larson, D.E., Shen, D., McLellan, M.D., Lin, L., Miller, C.A., Mardis, E.R., Ding, L., and Wilson, R.K. (2012). VarScan 2: somatic mutation and copy number alteration discovery in cancer by exome sequencing. Genome Res. *22*, 568–576.

Kolasinska-Zwierz, P., Down, T., Latorre, I., Liu, T., Liu, X.S., and Ahringer, J. (2009). Differential chromatin marking of introns and expressed exons by H3K36me3. Nat. Genet. *41*, 376–381.

Kouzarides, T. (2007). Chromatin modifications and their function. Cell *128*, 693–705.

Kuleshov, M.V., Jones, M.R., Rouillard, A.D., Fernandez, N.F., Duan, Q., Wang, Z., Koplev, S., Jenkins, S.L., Jagodnik, K.M., Lachmann, A., et al. (2016). Enrichr: a comprehensive gene set enrichment analysis web server 2016 update. Nucleic Acids Res. *44* (*W1*), W90–W97.

Lachmann, A., Xu, H., Krishnan, J., Berger, S.I., Mazloom, A.R., and Ma'ayan, A. (2010). ChEA: transcription factor regulation inferred from integrating genome-wide ChIP-X experiments. Bioinformatics *26*, 2438–2444.

Lachmann, A., Torre, D., Keenan, A.B., Jagodnik, K.M., Lee, H.J., Wang, L., Silverstein, M.C., and Ma'ayan, A. (2018). Massive mining of publicly available RNA-seq data from human and mouse. Nat. Commun. *9*, 1366.

Lai, Z., Markovets, A., Ahdesmaki, M., Chapman, B., Hofmann, O., McEwen, R., Johnson, J., Dougherty, B., Barrett, J.C., and Dry, J.R. (2016). VarDict: a novel and versatile variant caller for next-generation sequencing in cancer research. Nucleic Acids Res. *44*, e108.

Levine, A.J., Jenkins, N.A., and Copeland, N.G. (2019). The roles of initiating truncal mutations in human cancers: the order of mutations and tumor cell type matters. Cancer Cell *35*, 10–15.

Lewis, J.S., Lee, J.A., Underwood, J.C., Harris, A.L., and Lewis, C.E. (1999). Macrophage responses to hypoxia: relevance to disease mechanisms. J. Leukoc. Biol. *66*, 889–900.

Li, H., and Durbin, R. (2009). Fast and accurate short read alignment with Burrows-Wheeler transform. Bioinformatics *25*, 1754–1760.

Ligon, K.L., Alberta, J.A., Kho, A.T., Weiss, J., Kwaan, M.R., Nutt, C.L., Louis, D.N., Stiles, C.D., and Rowitch, D.H. (2004). The oligodendroglial lineage marker OLIG2 is universally expressed in diffuse gliomas. J. Neuropathol. Exp. Neurol. *63*, 499–509.

Ligon, K.L., Huillard, E., Mehta, S., Kesari, S., Liu, H., Alberta, J.A., Bachoo, R.M., Kane, M., Louis, D.N., Depinho, R.A., et al. (2007). Olig2-regulated lineage-restricted pathway controls replication competence in neural stem cells and malignant glioma. Neuron *53*, 503–517.

Liu, J., Merkle, F.T., Gandhi, A.V., Gagnon, J.A., Woods, I.G., Chiu, C.N., Shimogori, T., Schier, A.F., and Prober, D.A. (2015). Evolutionarily conserved regulation of hypocretin neuron specification by Lhx9. Development *142*, 1113–1124.

Mack, S.C., Witt, H., Piro, R.M., Gu, L., Zuyderduyn, S., Stütz, A.M., Wang, X., Gallo, M., Garzia, L., Zayne, K., et al. (2014). Epigenomic alterations define lethal CIMP-positive ependymomas of infancy. Nature *506*, 445–450.

Mack, S.C., Pajtler, K.W., Chavez, L., Okonechnikov, K., Bertrand, K.C., Wang, X., Erkek, S., Federation, A., Song, A., Lee, C., et al. (2018). Therapeutic targeting of ependymoma as informed by oncogenic enhancer profiling. Nature *553*, 101–105.

Mackay, A., Burford, A., Carvalho, D., Izquierdo, E., Fazal-Salom, J., Taylor, K.R., Bjerke, L., Clarke, M., Vinci, M., Nandhabalan, M., et al. (2017). Integrated molecular meta-analysis of 1,000 pediatric high-grade and diffuse intrinsic pontine glioma. Cancer Cell *32*, 520–537.e5.

Mar, B.G., Bullinger, L.B., McLean, K.M., Grauman, P.V., Harris, M.H., Stevenson, K., Neuberg, D.S., Sinha, A.U., Sallan, S.E., Silverman, L.B., et al. (2014). Mutations in epigenetic regulators including SETD2 are gained during relapse in paediatric acute lymphoblastic leukaemia. Nat. Commun. *5*, 3469.

McKenna, A., Hanna, M., Banks, E., Sivachenko, A., Cibulskis, K., Kernytsky, A., Garimella, K., Altshuler, D., Gabriel, S., Daly, M., and DePristo, M.A. (2010). The Genome Analysis Toolkit: a MapReduce framework for analyzing next-generation DNA sequencing data. Genome Res. *20*, 1297–1303.

Modena, P., Lualdi, E., Facchinetti, F., Veltman, J., Reid, J.F., Minardi, S., Janssen, I., Giangaspero, F., Forni, M., Finocchiaro, G., et al. (2006). Identification of tumor-specific molecular signatures in intracranial ependymoma and association with clinical characteristics. J. Clin. Oncol. *24*, 5223–5233.

Müller, S., Kohanbash, G., Liu, S.J., Alvarado, B., Carrera, D., Bhaduri, A., Watchmaker, P.B., Yagnik, G., Di Lullo, E., Malatesta, M., et al. (2017). Single-cell profiling of human gliomas reveals macrophage ontogeny as a basis for regional differences in macrophage activation in the tumor microenvironment. Genome Biol. *18*, 234.

Novitch, B.G., Chen, A.I., and Jessell, T.M. (2001). Coordinate regulation of motor neuron subtype identity and pan-neuronal properties by the bHLH repressor Olig2. Neuron *31*, 773–789.

Nowakowski, T.J., Bhaduri, A., Pollen, A.A., Alvarado, B., Mostajo-Radji, M.A., Di Lullo, E., Haeussler, M., Sandoval-Espinosa, C., Liu, S.J., Velmeshev, D., et al. (2017). Spatiotemporal gene expression trajectories reveal developmental hierarchies of the human cortex. Science *358*, 1318–1323.

Ohlsson, R., Kanduri, C., Whitehead, J., Pfeifer, S., Lobanenkov, V., and Feinberg, A.P. (2003). Epigenetic variability and the evolution of human cancer. Adv. Cancer Res. *88*, 145–168.

Ohm, J.E., McGarvey, K.M., Yu, X., Cheng, L., Schuebel, K.E., Cope, L., Mohammad, H.P., Chen, W., Daniel, V.C., Yu, W., et al. (2007). A stem cell-like chromatin pattern may predispose tumor suppressor genes to DNA hypermethylation and heritable silencing. Nat. Genet. *39*, 237–242.

Ozawa, T., Arora, S., Szulzewsky, F., Juric-Sekhar, G., Miyajima, Y., Bolouri, H., Yasui, Y., Barber, J., Kupp, R., Dalton, J., et al. (2018). A de novo mouse model of C11orf95-RELA fusion-driven ependymoma identifies driver functions in addition to NF-κB. Cell Rep. *23*, 3787–3797.

Pajtler, K.W., Witt, H., Sill, M., Jones, D.T., Hovestadt, V., Kratochwil, F., Wani, K., Tatevossian, R., Punchihewa, C., Johann, P., et al. (2015). Molecular classification of ependymal tumors across all CNS compartments, histopathological grades, and age groups. Cancer Cell *27*, 728–743.

Paradis, E., Claude, J., and Strimmer, K. (2004). APE: analyses of phylogenetics and evolution in R language. Bioinformatics *20*, 289–290.

Parker, M., Mohankumar, K.M., Punchihewa, C., Weinlich, R., Dalton, J.D., Li, Y., Lee, R., Tatevossian, R.G., Phoenix, T.N., Thiruvenkatam, R., et al. (2014). C11orf95-RELA fusions drive oncogenic NF-κB signalling in ependymoma. Nature *506*, 451–455.

Parker, N.R., Hudson, A.L., Khong, P., Parkinson, J.F., Dwight, T., Ikin, R.J., Zhu, Y., Cheng, Z.J., Vafaee, F., Chen, J., et al. (2016). Intratumoral heterogeneity identified at the epigenetic, genetic and transcriptional level in glioblastoma. Sci. Rep. *6*, 22477.

Patel, A.P., Tirosh, I., Trombetta, J.J., Shalek, A.K., Gillespie, S.M., Wakimoto, H., Cahill, D.P., Nahed, B.V., Curry, W.T., Martuza, R.L., et al. (2014). Single-cell RNA-seq highlights intratumoral heterogeneity in primary glioblastoma. Science *344*, 1396–1401.

Peukert, D., Weber, S., Lumsden, A., and Scholpp, S. (2011). Lhx2 and Lhx9 determine neuronal differentiation and compartition in the caudal forebrain by regulating Wnt signaling. PLoS Biol. *9*, e1001218.

Rahat, M.A., Bitterman, H., and Lahat, N. (2011). Molecular mechanisms regulating macrophage response to hypoxia. Front. Immunol. *2*, 45.

Rétaux, S., Rogard, M., Bach, I., Failli, V., and Besson, M.J. (1999). Lhx9: a novel LIM-homeodomain gene expressed in the developing forebrain. J. Neurosci. *19*, 783–793.

Ricketts, C.J., De Cubas, A.A., Fan, H., Smith, C.C., Lang, M., Reznik, E., Bowlby, R., Gibb, E.A., Akbani, R., Beroukhim, R., et al.; Cancer Genome Atlas Research Network (2018). The Cancer Genome Atlas comprehensive molecular characterization of renal cell carcinoma. Cell Rep. *23*, 3698.

Ritchie, M.E., Phipson, B., Wu, D., Hu, Y., Law, C.W., Shi, W., and Smyth, G.K. (2015). limma powers differential expression analyses for RNA-sequencing and microarray studies. Nucleic Acids Res. *43*, e47.

Schlesinger, Y., Straussman, R., Keshet, I., Farkash, S., Hecht, M., Zimmerman, J., Eden, E., Yakhini, Z., Ben-Shushan, E., Reubinoff, B.E., et al. (2007). Polycomb-mediated methylation on Lys27 of histone H3 pre-marks genes for de novo methylation in cancer. Nat. Genet. *39*, 232–236.

Shihab, H.A., Gough, J., Cooper, D.N., Day, I.N.M., and Gaunt, T.R. (2013). Predicting the functional consequences of cancer-associated amino acid substitutions. Bioinformatics *29*, 1504–1510.

Szerlip, N.J., Pedraza, A., Chakravarty, D., Azim, M., McGuire, J., Fang, Y., Ozawa, T., Holland, E.C., Huse, J.T., Jhanwar, S., et al. (2012). Intratumoral heterogeneity of receptor tyrosine kinases EGFR and PDGFRA amplification in glioblastoma defines subpopulations with distinct growth factor response. Proc. Natl. Acad. Sci. USA *109*, 3041–3046.

Taylor, M.D., Poppleton, H., Fuller, C., Su, X., Liu, Y., Jensen, P., Magdaleno, S., Dalton, J., Calabrese, C., Board, J., et al. (2005). Radial glia cells are candidate stem cells of ependymoma. Cancer Cell *8*, 323–335.

Watkins, T.B.K., and Schwarz, R.F. (2018). Phylogenetic quantification of intratumor heterogeneity. Cold Spring Harb. Perspect. Med. *8*, a028316.

Weinhold, N., Jacobsen, A., Schultz, N., Sander, C., and Lee, W. (2014). Genome-wide analysis of noncoding regulatory mutations in cancer. Nat. Genet. *46*, 1160–1165.

Whitcher, B., Schmid, V.J., and Thornton, A. (2011). Working with the DICOM and NIfTI data standards in R. J. Stat. Soft. *44*, 1–29.

Widschwendter, M., Fiegl, H., Egle, D., Mueller-Holzner, E., Spizzo, G., Marth, C., Weisenberger, D.J., Campan, M., Young, J., Jacobs, I., and Laird, P.W. (2007). Epigenetic stem cell signature in cancer. Nat. Genet. *39*, 157–158.

Witt, H., Mack, S.C., Ryzhova, M., Bender, S., Sill, M., Isserlin, R., Benner, A., Hielscher, T., Milde, T., Remke, M., et al. (2011). Delineation of two clinically and molecularly distinct subgroups of posterior fossa ependymoma. Cancer Cell *20*, 143–157.

Yuan, W., Xu, M., Huang, C., Liu, N., Chen, S., and Zhu, B. (2011). H3K36 methylation antagonizes PRC2-mediated H3K27 methylation. J. Biol. Chem. *286*, 7983–7989.

Yung, W.K., Shapiro, J.R., and Shapiro, W.R. (1982). Heterogeneous chemosensitivities of subpopulations of human glioma cells in culture. Cancer Res. *42*, 992–998.

Zhong, S., Zhang, S., Fan, X., Wu, Q., Yan, L., Dong, J., Zhang, H., Li, L., Sun, L., Pan, N., et al. (2018). A single-cell RNA-seq survey of the developmental landscape of the human prefrontal cortex. Nature *555*, 524–528.

Zhou, Q., and Anderson, D.J. (2002). The bHLH transcription factors OLIG2 and OLIG1 couple neuronal and glial subtype specification. Cell *109*, 61–73.

STAR★METHODS

KEY RESOURCES TABLE

REAGENT or RESOURCE	SOURCE	IDENTIFIER
Antibodies		
MIB-1/Ki-67	Dako	GA626
L1CAM	Sigma	UJ127.11
GFAP	Dako	GA524
EMA	Leica	GP1.4
GFP	Abcam	ab6556
H3K36me3	Abcam	ab9050
Biological Samples		
Anaplastic ependymoma samples	UCSF Brain Tumor Center	N/A
Critical Commercial Assays		
TruSeq RNA Library Prep Kit v2	Illumina	RS-122- 2001
Nimblegen SeqCap EZ Human Exome Kit v3.0	Roche	06465684001
CellTiter 96 Non-Radioactive Cell Proliferation Assay	Promega	G4000
Deposited Data		
DNA Methylation Array	This paper	GEO: GSE142320
RNA-seq data	This paper	SRA: PRJNA597052
WES data	This paper	SRA: PRJNA597052
Experimental Models: Cell Lines		
Human: SF11435 ependymoma cell culture	UCSF Clinical Cancer Genomics Laboratory	SF11435
Oligonucleotides		
G-blocks	IDT	N/A
Genotyping: SETD2 forward 5′-TGTAAAACGACGG CCAGTCCTGTTACTCCTCGCGCCG-3′	This paper	N/A
Genotyping: SETD2 reverse 5′-CAGGAAACAGCTA TGACCGGTCAAGCCAACAGCTGCAA-3′).	This paper	N/A
SETD2 L1962P correction forward: 5′-GACGCTGA AATAGAGCCCAAAGAGAGCAACGGC-3′	This paper	N/A
SETD2 L1962P correction reverse: 5′-GCCGTTGC TCTCTTTGGGCTCTATTTCAGCGTC-3′	This paper	N/A
SETD2 K2R mutagenesis forward: 5′-TCCGCTAGCG CCACCATGAGGCAGCTGCAGCCGCAGCCGCCTCC-3′	This paper	N/A
SETD2 K2R mutagenesis reverse: 5′-GGAGGCGGCT GCGGCTGCAGCTGCCTCATGGTGGCGCTAGCGGA-3′	This paper	N/A
Recombinant DNA		
SETD2-EGFP	This paper	N/A
SETD2^{K2R}-EGFP	This paper	N/A
C11orf95	BACPAC Resources	CH17-67K13; CH17-388O01
RELA	BACPAC Resources	RP11-642F7; CH17-211O12
YAP1	BACPAC Resources	RP11-11N20; RP11-1082I13
Software and Algorithms		
3D Slicer v4.8.0	https://www.slicer.org	https://www.slicer.org
R v3.4.3	https://www.r-project.org	https://www.r-project.org
oro.dicom v0.5.3	Whitcher et al., 2011	https://cran.r-project.org/web/packages/oro.dicom

(Continued on next page)

Continued

REAGENT or RESOURCE	SOURCE	IDENTIFIER
Kallisto v0.43.1	Bray et al., 2016	https://pachterlab.github.io/kallisto/
JAFFA v1.09	Davidson et al., 2015	https://github.com/Oshlack/JAFFA/
Tophat v2.1.0	Kim et al., 2013	http://ccb.jhu.edu/software/tophat/
Minfi v1.30.0	Aryee et al., 2014; Fortin et al., 2017	https://bioconductor.org/packages/release/bioc/html/minfi.html
Limma v3.40.0	Ritchie et al., 2015	https://bioconductor.org/packages/release/bioc/html/limma.html
Conumee v1.3.0	https://bioconductor.org/packages/release/bioc/html/conumee.html	https://bioconductor.org/packages/release/bioc/html/conumee.html
Bcbio	https://github.com/bcbio/bcbio-nextgen	https://github.com/bcbio/bcbio-nextgen
Picard suite	http://broadinstitute.github.io/picard	http://broadinstitute.github.io/picard
Genome Analysis Toolkit	McKenna et al., 2010	https://software.broadinstitute.org/gatk/
Varscan2 v2.4.0	Koboldt et al., 2012	http://dkoboldt.github.io/varscan/
Freebayes	Garrison and Marth, 2012	https://github.com/ekg/freebayes
Vardict	Lai et al., 2016	https://github.com/AstraZeneca-NGS/VarDict
Snpeff v4.3	Cingolani et al., 2012	http://snpeff.sourceforge.net
Sequenza v2.1.0	Favero et al., 2015	https://cran.r-project.org/web/packages/sequenza/index.html
Ape v5.0	https://cran.r-project.org/web/packages/ape	https://cran.r-project.org/web/packages/ape

LEAD CONTACT AND MATERIALS AVAILABILITY

SETD2 mutant constructs are available upon request. Cell lines (SF11435) are available upon request. Further information and requests for resources and reagents should be directed to and will be fulfilled by the Lead Contact, David R. Raleigh (david.raleigh@ucsf.edu).

EXPERIMENTAL MODEL AND SUBJECT DETAILS

Cell Culture

SF11435 cells (male) were maintained at $37°C$ in a 5% CO_2 atmosphere with 21% oxygen, and grown in a 1:1 ratio of DMEM/F12 (Life Technologies, Carlsbad, CA) and Neurobasal medium (Life Technologies) supplemented with 5% FBS (Life Technologies), B-27 supplement without vitamin A (Life Technologies), N-2 supplement (Life Technologies), 1X GlutaMAX (Life Technologies), 1mM NEAA (Life Technologies), 100U/mL Anti-Anti (Life Technologies), 20ng/mL EGF (R&D systems, Minneapolis, MN), 20ng/mL FGF2 (Peprotech, Rocky Hill). Cell lines were validated using short-tandem repeat profiling at the UCSF Clinical Cancer Genomics Laboratory.

Tumor sample acquisition

A 29 year old male patient was taken to the operating room for a fronto-parietal parasagittal craniotomy for tumor resection. The preoperative stereotactic magnetic resonance images (MRI) were registered to physical space using the stereotactic neuronavigation system (BrainLab®, Munich, Germany). The accuracy of the registration was confirmed using anatomic landmarks. Surgical resection of the tumor was carried out in the usual manner. Throughout the resection, fresh tissue samples were obtained. The location of each sample (including a screenshot and DICOM coordinates) was collected using the stereotactic probe immediately prior to collecting the sample. Once collected from the single tumor, each of the six regional samples were immediately passed off the surgical field and placed into liquid nitrogen for subsequent analysis.

METHOD DETAILS

Quantitative imaging analysis

Preoperative MR imaging was performed on a 3.0 tesla scanner (Discovery; GE Healthcare, Waukesha, WI) using a neuronavigation protocol that included 3D volumetric structural sequences without and with gadolinium contrast as well as axial diffusion tensor imaging (DTI) and axial arterial spin labeling (ASL) perfusion imaging encompassing the brain.

The preoperative stereotactic MRI was imported into 3D Slicer v4.8.0. The brain and tumor were each segmented using the editor module, and the tumor volume was quantified using the label statistics module. DICOM coordinates collected from the stereotactic neuronavigation system were entered into the markups module and used to generate a 3D model of the tumor with sample sites. Regions of interest (ROI) were created around each point and used for downstream image analysis.

For radiographic characterization of the tumor and each spatially-defined sample, the 3D T1 post-gadolinium, DTI, and ASL images were transferred to a commercially available software system (AW Server; GE Healthcare) for diffusion and perfusion processing and analysis. Mean diffusivity (MD) and fractional anisotropy (FA) maps were generated on a voxel-by-voxel basis from the DTI imaging dataset. For ASL perfusion calculations, cerebral blood flow (CBF) maps were also created on a voxel-by-voxel basis. The 3D T1 post-gadolinoum images were aligned to the same axial location as the MD, FA, and CBF maps. To account for tissue shifts and sampling margin of error, 100 mm^3 spherical ROIs were manually delineated about the six annotated sampling sites. Once validated, ROIs were transferred to MD, FA, and CBF maps to allow for collection of quantitative diffusion and perfusion metrics.

Sample distance metric analysis

DICOM files corresponding to the tumor and sample ROIs were imported using the oro.dicom package in the R statistical environment (Whitcher et al., 2011). Pairwise distances of samples from one another, as well the minimum pairwise distance from each sample to the tumor's periphery and centroid, were calculated from DICOM coordinates. Heatmaps of sample distances were generated using the gplots R package.

Tissue processing and immunohistochemistry

Immunohistochemical (IHC), and hematoxylin and eosin (H&E) stains were performed on formalin-fixed, paraffin embedded tissue sections at the University of California San Francisco Immunohistochemistry Laboratory and the University of California San Francisco Neuropathology Brain Tumor Center Biomarkers Laboratory. Primary antibodies used were as follows: MIB-1/Ki-67 (MIB-1, Dako, Glostrup, Denmark, 1:50 dilution), L1CAM (clone UJ127.11, Sigma, St Louis, MO, 1:3000 dilution), GFAP (Polyclonal, Dako, 1:3000 dilution) and EMA (clone GP1.4, Leica, Newcastle Upon Tyne, United Kingdom, prediluted). All staining was performed in Ventana or Leica Bond automated staining processors.

Fluorescence *In Situ* Hybridization (FISH)

Dual-color FISH was performed on 4 μm paraffin embedded tissue sections. Probes were derived from BAC clones (BACPAC Resources, Oakland, CA) and labeled with either AlexaFluor-488 or AlexaFluor-555 fluorochromes. BAC clones were used to develop break apart probes for the following genes: *C11orf95* (CH17-67K13 & CH17-388O01), *RELA* (RP11-642F7 & CH17-211O12), and *YAP1* (RP11-11N20 & RP11-1082I13). Probes were co-denatured with the target cells on a slide moat at 90°C for 12 minutes. The slides were incubated overnight at 37°C on a slide moat and then washed in 4M Urea/2xSSC at 25°C for 1 minute. Nuclei were counterstained with DAPI (200ng/ml, Vector Labs, Burlingame, CA) for viewing on an Olympus BX51 fluorescence microscope equipped with a 100-W mercury lamp; FITC, Rhodamine, and DAPI filters; 100X PlanApo (1.40) oil objective; and a Jai CV digital camera. Images were captured and processed using the Cytovision software (Leica Biosystems, Richmond, IL).

RNA-seq

RNA was isolated from tumor samples using the AllPrep DNA/RNA/miRNA Universal Kit (QIAGEN, Valencia, CA). Library preparation was performed using the TruSeq RNA Library Prep Kit v2 (RS-122- 2001, Illumina, San Diego, CA) and 50 bp single end reads were sequenced on an Illumina HiSeq 2500 to a mean of 7 million reads per sample at the Center for Advanced Technology at the University of California San Francisco. Quality control of FASTQ files was performed with FASTQ. Transcript abundances were quantified using Kallisto version 0.43.1 with the flags '-b 100–single -t 10 -l 200 -s 50' using GENCODE release 26, based on GRCh38 (Bray et al., 2016; Harrow et al., 2012; Kim et al., 2013). Principal component analysis was performed in the statistical environment R version 3.4.3 using the base command 'prcomp' with the parameters 'center = TRUE, scale. = FALSE' on log2 transformed transcripts per million (TPM) values with a pseudocount of 1. Genes were ranked by the absolute value of the maximum gene loading scores in PCA space among the first three principal components, which was determined based on diminishing variance explained in principal components four and greater. Hierarchical clustering was performed using complete linkage hierarchical clustering using the log2 transformed TPM values with pseudocount of 1. The top 250 most variable genes in principal components 1 to 3 were used for clustering, and cluster assignments were robust to both linkage method (average or complete linkage) and also number of genes used. Identical clusters were obtained using up to 10,000 variable genes for clustering analysis.

Analysis of developmental gene expression signatures was performed by obtaining cell type specific markers from Zhong et al. (2018) and overlapping this gene list with the top 2,500 most variable genes from PCA in our analysis. The mean TPM expression of the remaining cell type specific genes for each of the cell types described in Zhong et al. (2018) was calculated for each of the ependymoma regions. The log2 transformed TPM values were then clustered by complete linkage hierarchical clustering.

Gene ontology analysis was performed using Enrichr, and p values displayed were multiple hypothesis corrected adjusted p values (Chen et al., 2013). PRC2 target genes were obtained from the ChIP enrichment analysis (ChEA) database release 2016 (Lachmann et al., 2010) by filtering the gene lists for those containing EZH2, SUZ12, or EED in their titles.

Fusion gene analysis using RNA-seq reads was performed using two independent fusion gene detectors. JAFFA version 1.09 was executed using the flags 'readLayout = single' against the merged fastq files for all ependymoma regions (Davidson et al., 2015). The fusion detection function of Tophat version 2.1.0 was executed using the flags '–bowtie1–no-coverage-search–fusion-search' against the merged fastq files for all ependymoma regions, using the GRCh38 reference annotation.

DNA Methylation Arrays

Genomic DNA was isolated from tumor samples using the AllPrep DNA/RNA/miRNA Universal Kit (QIAGEN, Valencia, CA). DNA (1000 ng) is bisulfite converted using the Zymo EZ DNA methylation kit (Zymo Research, Irvine, CA) according to the manufacturer's recommendations. The amount of bisulfite-converted DNA as well as the completeness of bisulfite conversion for each sample are assessed using a panel of MethyLight-based real-time PCR quality control assays. Bisulfite-converted DNA is then used as a substrate for the Illumina EPIC BeadArrays. Each sample is whole genome amplified (WGA) and then enzymatically fragmented. Samples are then hybridized overnight to an 8-sample BeadArray, in which the WGA-DNA molecules anneal to locus-specific DNA oligomers linked to individual bead types. Adenine and thymine nucleotides are labeled with cy5 (red), while cytosine nucleotides are labeled with cy3 (green). BeadArrays are scanned and the raw signal intensities are extracted from the *.IDAT files using the 'noob' function in the *minfi* R package (Aryee et al., 2014; Fortin et al., 2017). Only probes with detection $p < 0.05$ in all samples were included for further analysis. Data were normalized using functional normalization (Fortin et al., 2014). Probes were filtered based on the following criteria: (i) removal of probes targeting the X and Y chromosomes (n = 11,551), (ii) removal of probes containing a common single nucleotide polymorphism (SNP) within the targeted CpG site or on an adjacent basepair (n = 24,536), and (iii) removal of probes not mapping uniquely to the hg19 human reference genome (n = 9,993). A total of 815,630 probes were retained for further analysis. Principal component analysis was performed in the statistical environment R version 3.4.3 using the base command 'prcomp' with the parameters 'center = TRUE, scale. = FALSE' against the normalized β enrichment values (β = methylated/[methylated+unmethylated]). Complete linkage hierarchical clustering was performed using the top 2,000 most variable probes, based on their absolute value of gene loading scores in the first three principal components, across all ependymoma samples. For probe-level differential methylation analysis, the limma Bioconductor package was used to fit a linear model accounting for the paired nature of the data with a FDR < 0.001 considered significant (Ritchie et al., 2015). β values were used for visualization of methylation levels and M values were used for statistical analysis (M = log2[methylated/unmethylated]) (Du et al., 2010). Sample type classification was performed using the random forest classifier of DNA methylation profiles on the Molecular Neuropathology web portal (Capper et al., 2018). CNV profiles from DNA methylation data were generated as described previously (Capper et al., 2018) using the *conumee* R package v.1.3.0. Segments with combined probe intensities greater than 0.05 or less than −0.05 log2 ratio compared to 2 sets of 50 control tissues with balanced chromosome profiles (Capper et al., 2018) were identified as either gain or loss, respectively.

Whole exome sequencing

Library preparation, exome capture and sequencing were performed at the Institute for Human Genetics at the University of California San Francisco. Sequencing libraries were prepared using the Kapa Hyper Prep Kit and exome capture was performed with the Nimblegen SeqCap EZ Human Exome Kit v. 3.0. Paired end sequencing with read length 100 base pairs was performed on the Illumina HiSeq4000. All subsequent data analysis was performed with the *bcbio* pipeline with default parameters [https://github.com/bcbio/bcbio-nextgen]. Reads were aligned with the Burrows-Wheeler aligner (Li and Durbin, 2009) to the reference human genome (build hg19). Only uniquely aligned reads were included for further processing with the Picard suite (http://broadinstitute.github.io/picard/) and the Genome Analysis Toolkit (McKenna et al., 2010) for de-duplication, local realignment and base quality score recalibration. Alignment quality metrics were calculated with the Picard suite. Somatic variants (point mutations, small indels) were identified from matched tumor-normal samples using Varscan2 (Koboldt et al., 2012), Freebayes (Garrison and Marth, 2012) and Vardict (Lai et al., 2016) at a significance threshold $p < 0.05$, and results from each algorithm were merged into a single Ensemble callset including only those significant hits identified in at least 2 callers. Hits were further filtered based on quality metrics using default parameters including (i) mean base quality > 25, (ii) > 5 reads in tumor and normal sample, (iii) > 10% variant reads in tumor, (iv) > 90% reference reads in normal, and (v) strand bias. Variants were annotated using Snpeff v4.3 (Cingolani et al., 2012)and were further filtered to only include those marked as high, moderate or low priority and occurring in protein coding or splice site locations. Annotations were obtained by querying the COSMIC database (Forbes et al., 2017). Ploidy, cellularity analysis, and chromosome segmentation was performed using Sequenza version 2.1.0 (Favero et al., 2015) using default parameters against reads above quality score of 20. Segmentation output from Sequenza were then used for generation of CNV profiles from whole exome sequencing data using default parameters (Favero et al., 2015).

Sanger sequencing

Samples were genotyped for the *SETD2* mutation to validate whole exome sequencing reads. The first exon of *SETD2* was PCR amplified using the GC-RICH PCR System (Roche Applied Science, Pleasanton, CA). PCR was performed with the *SETD2*-forward (5′-TGTAAAACGACGGCCAGTCCTGTTACTCCTCGCGCCG-3′) and *SETD2*-reverse primers (5′-CAGGAAACAGCTATGACCGGT CAAGCCAACAGCTGCAA-3′). The amplification profile was 40 cycles of denaturing at 95°C, annealing at 60°C, and extension at 72°C. PCR products were purified using the QIAGEN Gel Extraction kit, and submitted for Sanger sequencing with the M13-forward sequencing primer (5′-TGTAAAACGACGGCCAGT-3′).

Phylogenetic analysis

Binary mutation calls were used to build a distance matrix across all samples using the Manhattan distance metric, including a normal tissue sample for which all mutations were absent. A phylogenetic tree was constructed using an ordinary least-squares minimum evolution approach (Desper and Gascuel, 2002) from the *APE* R package (Paradis et al., 2004). Each branch of the resulting tree was annotated with the total number of mutations attributed to that branch.

SETD2 cloning

Full-length SETD2 was initially cloned into a CMV-Eos2.1 vector backbone to generate SETD2-Eos2.1. A custom G-block was used to generate the coding sequence of the N-terminal 503 amino acids of SETD2 (Integrated DNA Technologies, Coralville, IA), which was fused to the coding sequence C-terminal 2062 amino acids from SETD2-GFP (Addgene, Cambridge, MA) by restriction ligation of NheI and AgeI sites. An internal missense mutation (L1962P) was corrected using the QuikChange Lightning Site-Directed Mutagenesis Kit (Agilent Technologies, Santa Clara, CA) per the manufacturer's protocol with the following primers: 5′-GACGCTGAAATAGAGCCCA AAGAGAGCAACGGC-3′ and 5′-GCCGTTGCTCTCTTTGGGCTCTATTTCAGCGTC-3′. The K2R substitution was also introduced using the QuikChange Lightning Site-Directed Mutagenesis Kit per the manufacturer's protocol with the following primers: 5′-TCCGC TAGCGCCACCATGAGGCAGCTGCAGCCGCAGCCGCCTCC-3′ and 5′-GGAGGCGGCTGCGGCTGCAGCTGCCTCATGGTGGCGC TAGCGGA-3′. For experimentation, the complete SETD2 coding sequences either with or without the K2R substitution were moved to pLMJ1, a viral vector suitable for mammalian transduction which affixed a C-terminal EGFP tag onto each SETD2 construct.

Microscopy and proliferation assays

For microscopy, SF11435 cells were grown on glass coverslips and transduced with either wild-type SETD2-EGFP or SETD2^{K2R}-EGFP using polybrene at 70% confluency. Forty-eight hours post transfection, cells were fixed in 4% PFA for 8 minutes, blocked in 2.5% FBS, 200mM glycine, and 0.1% Triton X-100 in PBS for 30 minutes, incubated with anti-GFP and anti-H3K36me3 (Abcam, Cambridge, UK) primary antibodies overnight at 4°C, washed, and incubated with Alexa Fluor secondary antibodies (Thermo Fischer Scientific, Waltham, MA) for 1 hour at room temperature. Hoechst 3342 (Life Technologies) was added to the secondary antibody incluation to mark DNA. Following a final wash, cells were mounted in ProLong Diamond Antifade Mountant (Thermo Fischer Scientific), and immunofluorescence images were collected using a Zeiss 780 confocal microscope system (Carl Zeiss AG, Oberkochen, Germany).

For cell proliferation assays, SF11435 cells were grown in a 96-well plate and transduced with either wild-type SETD2-EGFP or SETD2^{K2R}-EGFP using polybrene at 50% confluency. Forty-eight hours post-transfection, cell proliferation was assayed using the CellTiter 96 Non-Radioactive Cell Proliferation Assay and a GloMax Discovery plate reader per the manufacturer's protocols (Promega, Madison, WI).

QUANTIFICATION AND STATISTICAL ANALYSIS

For Figures 2A–2C, 3A, S3, and S4A analysis is described above in section "DNA Methylation Arrays."

For Figures 2D, 3D, and 3J, analysis is described above in section "RNA-seq."

For Figure 2H, boxplots demonstrate median with first and third quartiles, whiskers represent 1.5*IQR. Tests of significance using the non-parametric Kolmogorov-Smirnov test, described in figure legends, to account for non-normally distributed data.

For Figure 3B, analysis is described above in section "Phylogenetic Analysis."

For Figures 3C and S4E, analysis is described above in section "Whole exome sequencing."

For Figure 3F, Signal intensities were quantified from 2D maximum intensity projections using ImageJ by outlining nuclei and measuring the integrated density of SETD2 fluorescent fusion proteins relative to total cellular integrated density.

For Figures 3E and 3G–3I, data are representative of 3 biologic replicates and are normalized to cells with WT overexpression, except that nuclear H3K36me3 nuclear intensity was normalized to cells transfected with empty vector. Tests of significance performed with Student's t test, described in figure legends.

For Figure 4, SETD2 mutational status was queried on the cBioportal in 42,199 pan-cancer samples (curated set of all non-redundant samples) (Gao et al., 2013). Samples were then stratified by those with WT SETD2 or those with any alteration in SETD2 (including in-frame, missense, truncating, fusion, amplification, or deep deletion mutation). Overall survival was performed using Kaplan-Meier analysis, and significance calculated using the log rank test. Described in main text and figure legends.

For Figure S1, analysis is described in above section "Sample distance metric analysis."

For Figures S2D and S4G Gene ontology analysis was performed using Enrichr, and p values displayed were multiple hypothesis corrected adjusted p values (Chen et al., 2013).

For Figure S4B, Gene ontology analysis of differentially methylated regions was performed using the Genomic Regions Enrichment of Annotations Tool (GREAT) using default settings.

DATA AND CODE AVAILABILITY

Methylation array data are deposited at GEO accession GEO: GSE142320. RNA-seq and whole exome-seq data are deposited at SRA accession PRJNA597052.

Supplemental Information

Multiplatform Molecular Profiling

Reveals Epigenomic Intratumor

Heterogeneity in Ependymoma

S. John Liu, Stephen T. Magill, Harish N. Vasudevan, Stephanie Hilz, Javier E. Villanueva-Meyer, Sydney Lastella, Vikas Daggubati, Jordan Spatz, Abrar Choudhury, Brent A. Orr, Benjamin Demaree, Kyounghee Seo, Sean P. Ferris, Adam R. Abate, Nancy Ann Oberheim Bush, Andrew W. Bollen, Michael W. McDermott, Joseph F. Costello, and David R. Raleigh

Figure S1, Related to Figure 1. Stereotactic mapping of an anaplastic ependymoma with C11orf95-RELA fusion.

A

Distance to periphery (mm)
A	2.5
B	1.1
C	1.9
D	1.5
E	3.2
F	4.5

B

Distance to centroid (mm)
A	18.4
B	20.0
C	22.8
D	26.8
E	13.1
F	7.5

C

Intersample distances (mm)

	A	B	C	D	E	F	
	0	10.93	32.12	33.97	19.65	16.89	A
	10.93	0	31.45	31.64	16.03	15.25	B
	32.12	31.45	0	7.32	14.49	16.86	C
	33.97	31.64	7.32	0	16.1	20.51	D
	19.65	16.03	14.49	16.1	0	6.38	E
	16.89	15.25	16.86	20.51	6.38	0	F
	A	B	C	D	E	F	
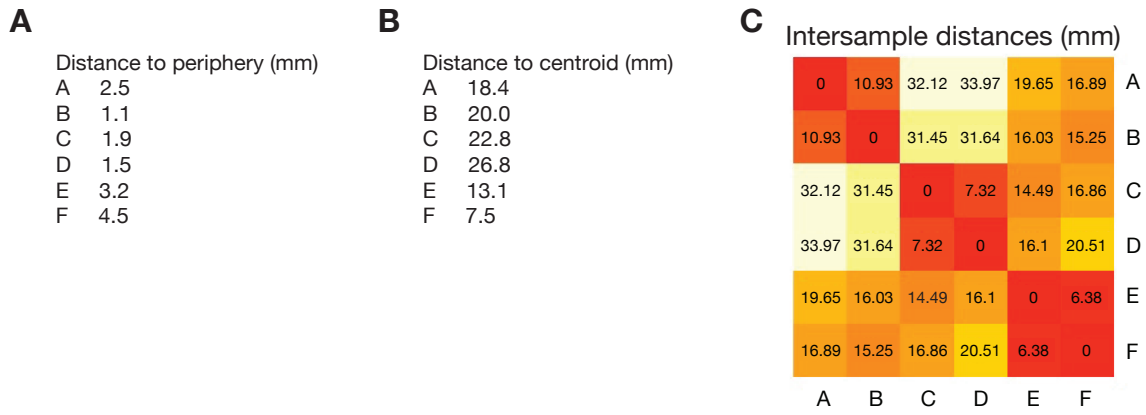
(A, B) Spatial mapping of tumor contour with defined sample coordinates in relation to the tumor periphery (A) and tumor centroid (B) measured in millimeters. (C) Pairwise distance matrix between samples measured in millimeters.
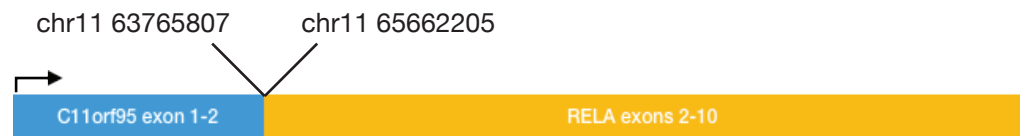
Figure S2, Related to Figure 2. Genomic and radiologic characterization of an anaplastic ependymoma with C11orf95-RELA fusion.
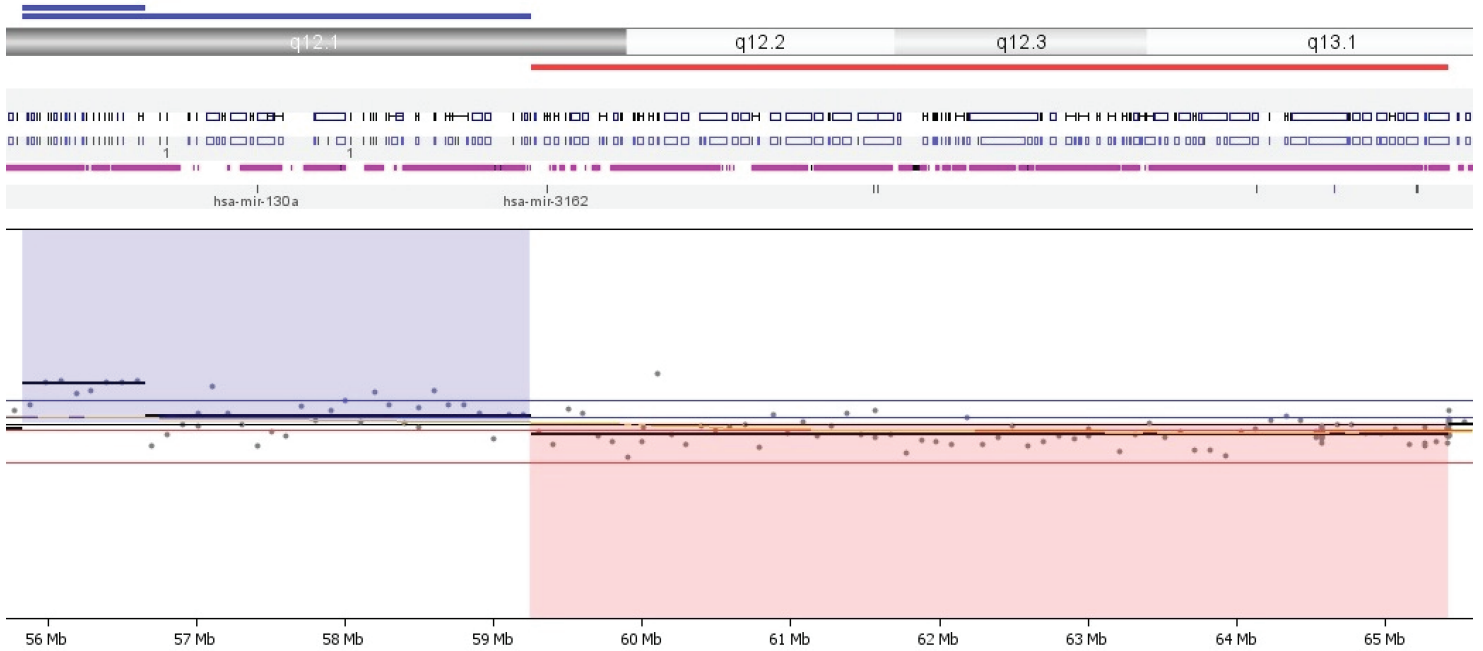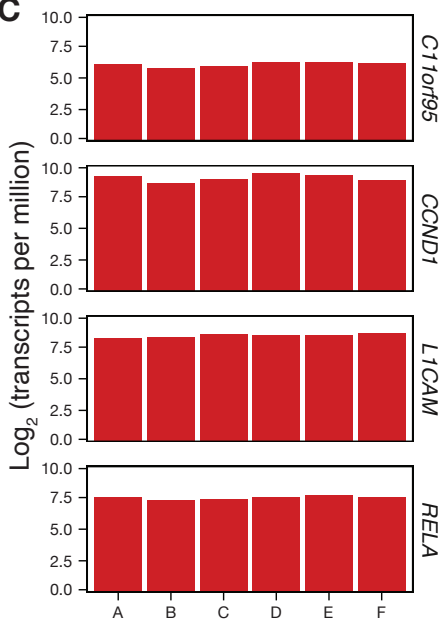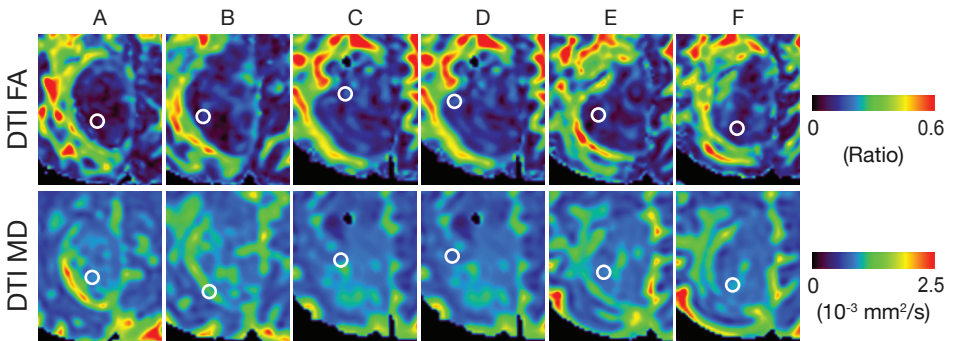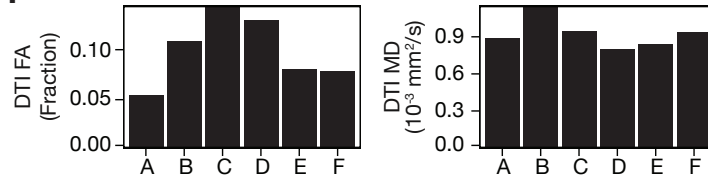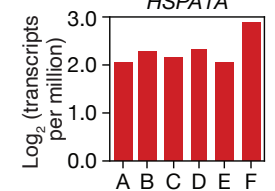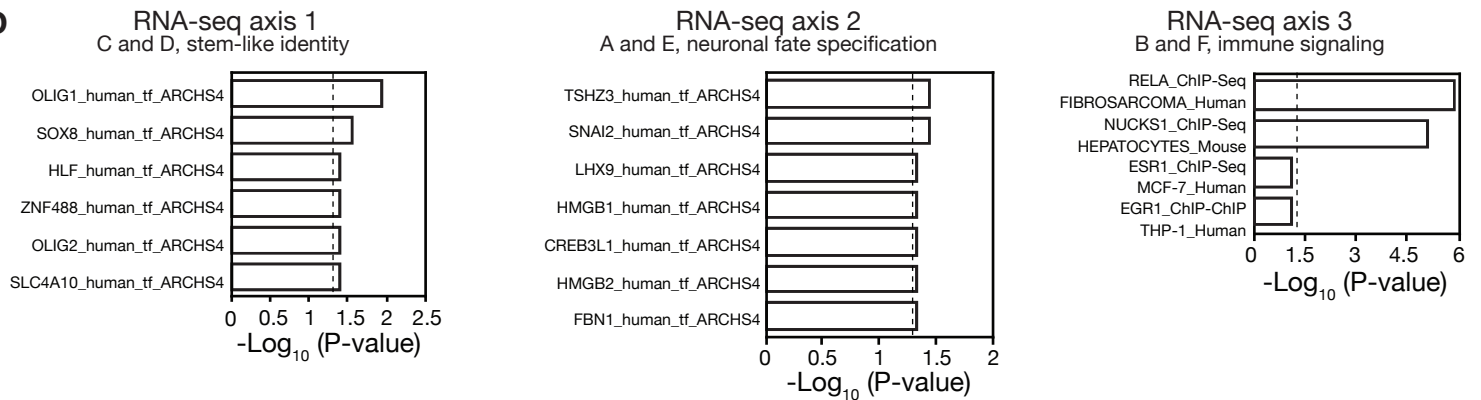
(A) Segmental chromosome 11q deletions and amplifications detected on targeted DNA sequencing, consistent with chromothripsis. (B) Number of exon junction spanning reads supporting C11orf95-RELA fusion as detected by JAFFA and Tophat Fusion (left), and gene fusion schematic with hg38 genomic coordinates (right). (C) Expression of ependymoma markers from RNA-seq reveals uniform enrichment of C11orf95-RELA target genes across samples. (D) Gene ontology analysis shows distinct enrichment patterns of stem-like, neuronal fate specification and immune signaling genes in stereotactic samples. (E, F) Quantitative MRI measurements of stereotactically-defined regions demonstrates enhanced fractional anisotropy in samples with stem-like identity (C and D). White circles indicate stereotactic sample locations. DTI, diffusion tensor imaging; FA, fractional anisotropy; MD, mean diffusivity; MRI, magnetic resonance imaging. (G) RNA-seq expression of the hypoxia gene HSPA1A across samples shows enrichment in sample F, the sample closest to the tumor centroid.

Figure S3, Related to Figure 2. Differences in cerebral blood flow drive intratumor heterogeneity within an anaplastic ependymoma with C11orf95-RELA fusion.
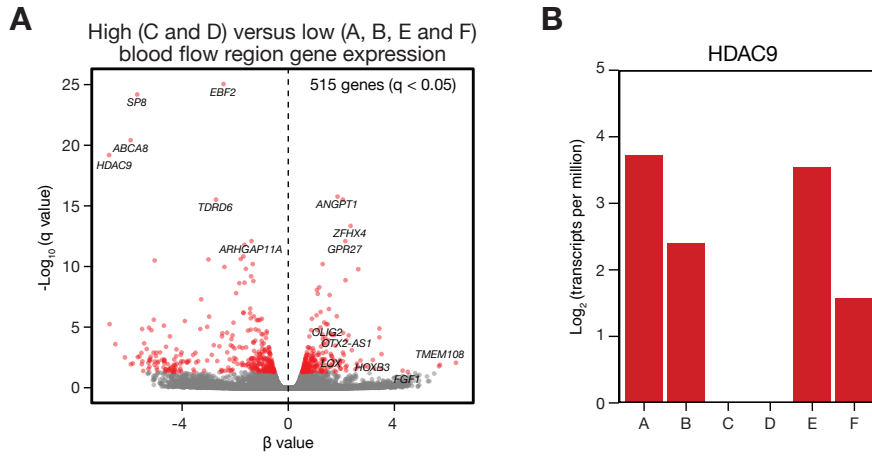
(A) Differential RNA-seq expression analysis of high versus low blood flow regions reveals 515 significantly expressed genes.
(B) RNA-seq expression of the histone deacetylase gene HDAC9 across samples shows depletion in samples C and D, the samples with the highest blood blow.

Figure S4, Related to Figure 3. Intratumor heterogeneity within an anaplastic ependymoma with C11orf95-RELA fusion.

A DNA methylation
Principal component analysis

B Hypomethylated probes in samples C and D

retrograde transport, endosome to Golgi
primitive hemopoiesis
somatic stem cell maintenance
positive regulation of mRNA catabolic process, deadenylation-dependent decay
central nervous system neuron development
embryonic hemopoiesis
anterior commissure morphogenesis
positive regulation of mRNA catabolic process
embryonic skeletal system morphogenesis
regulation of B cell differentiation

$-Log_{10}$ (FDR)

C DNA methylation

	Classifier	Score
Sample A	EPN, RELA	0.992
Sample B	EPN, RELA	0.993
Sample C	EPN, RELA	0.997
Sample D	EPN, RELA	0.998
Sample E	EPN, RELA	0.995
Sample F	EPN, RELA	0.992

D Whole exome sequencing

	Cellularity	Ploidy
Sample A	0.90	3.5
Sample B	0.75	3.5
Sample C	0.78	3.5
Sample D	0.89	3.4
Sample E	0.83	3.5
Sample F	0.85	3.5

E

Normal

WES
Copy number variant phylogeny

11
chr5,6,7,11q,14,16, 17,19,20,21 gain; chr9 loss

D   C

chr11p gain 1   1 chr13 loss

chr15 gain,
chr4 mid loss,   3
chr9p mid deep loss (CDKN2A)

B,E

chr4 gain 1

A,F

clonal
shared
private

F

C
↑
Nucleic acid sequence   3' C A G C T G C T T C A T C G G 5'
Protein sequence   Leu Gln Lys Met
↓
Arg

Blood

Sample A

Sample B

Sample C

Sample D

Sample E

Sample F

G RNA-seqnecing
Axis 2 (A and E) ChEA Genes

SUZ12_ChIP-Seq_MEFs_Mouse
SUZ12_ChIP-Seq_MESCs_Mouse
PAX3-FKHR_ChIP-Seq RHABDOMYOSARCOMA_Human
EZH2_ChIP-Seq_MESCs_Mouse
RNF2_ChIP-Seq_MESCs_Mouse
JARID2_ChIP-Seq_MESCs_Mouse
TRIM28_ChIP-Seq_HEK293_Human
EED_ChIP-ChIP_MESCs_Mouse

$-Log_{10}$(P-value)

(A) PCA of DNA methylation profiles reveals 69% percent of variation is explained by the first two principal components (PC). (B) Genomic Regions Enrichment of Annotations Tool (GREAT) gene ontology analysis of hypomethylated probes in samples and D is consistent with expression of stem cell genes. (C) DNA methylation profile based classification reveals RELA ependymoma in each sample (Capper et al., 2018). (D) Cellularity and ploidy results from Sequenza analysis demonstrates equivalent tumor composition in each sample. (E) Intratumor phylogeny based on clonal ordering of copy number variants derived from exome sequencing suggests that chromosomal structural alterations are an early event during ependymoma tumorigenesis. The number and identify of copy number variants defining each axis are indicated. (F) Sanger sequencing of SETD2 exon 1 reveals 5A>G (p.K2R) missense substitution in all tumor samples. (G) Chromatin Enrichment Analysis (ChEA) gene ontology of the top 200 genes in axis 2 from RNA-seq PCA shows enrichment for targets of SUZ12 and EZH2. Vertical dashed line corresponds to P=0.05.